KINETICS STUDY FOR FISCHER-TROPSCH SYNTHESIS OVER COBALT CATALYST BY KINETIC MONTE-CARLO SIMULATION

Nuttawut Pugingna

A Thesis Submitted in Partial Fulfilment of the Requirements
for the Degree of Master of Science
The Petroleum and Petrochemical College, Chulalongkorn University
in Academic Partnership with
The University of Michigan, The University of Oklahoma,
Case Western Reserve University, and Institut Français du Pétrole
2018

Thesis Title:	Kinetics Study for Fischer-Tropsch Synthesis over Cobalt Catalyst by Kinetic Monte-Carlo Simulation
By:	Nuttawut Pugingna
Program:	Petroleum Technology
Thesis Advisors:	Prof. Boonyarach Kitiyanan
	Prof. Robert M. Ziff

Accepted by The Petroleum and Petrochemical College, Chulalongkorn University, in partial fulfilment of the requirements for the Degree of Master of Science.

..... College Dean
(Prof. Suwabun Chirachanchai)

Thesis Committee:

.....
(Prof. Boonyarach Kitiyanan)

.....
(Prof. Robert M. Ziff)

.....
(Asst. Prof. Kitipat Siemanond)

.....
(Dr. Sitthiphong Pengpanich)

ABSTRACT

6073003063: Petroleum Technology Program
Nuttawut Pugingna: Kinetics Study for Fischer-Tropsch Synthesis over Cobalt Catalyst by Kinetic Monte-Carlo Simulation
Thesis Advisor: Prof. Boonyarach Kitiyanan, and Prof. Robert M. Ziff
80 pp.
Keyword: Kinetic Monte-Carlo simulation/ Fischer-Tropsch synthesis/ Reaction mechanism/ Process conditions

Kinetic Monte-Carlo simulation was utilized to study the kinetic behaviors of C_1 and C_2 formation in the Fischer-Tropsch synthesis over the cobalt surface by varying reaction conditions. Two reaction models: the carbide mechanism and the CO insertion mechanism were applied to this simulation. The production rates and fractional coverages of each adsorbed species could be calculated under the steady state. Moreover, the combination between carbide and CO insertion mechanism was also studied to suggest the possibility of each reaction mechanism, and compared the results with the reported experimental results under the same conditions. It was observed that the C–C bond formation was mainly performed through the insertion of adsorbed CO into a metal–methyl bond. Based on the CO insertion mechanism, the results obviously presented that the process conditions essentially influenced on the reactivity and selectivity of the reaction. The system exhibited non-reactive regions at the temperature below 463 K and the H_2/CO feed molar ratio lower than 1.1. In the steady reactive states, the surface is predominantly covered with adsorbed H and CO, and played an important role in the hydrocarbon chain growth.

บทคัดย่อ

ณัฐวุฒิ ภูกิ่งนา : การศึกษาจลนพลศาสตร์สำหรับปฏิกิริยาสังเคราะห์ฟิชเชอร์-โทรปช์บนตัวเร่งปฏิกิริยาโคบอลท์ด้วยแบบจำลองมอนติคาร์โลเชิงจลนพลศาสตร์ (Kinetics Study for Fischer-Tropsch Synthesis over Cobalt Catalyst by Kinetic Monte-Carlo Simulation) อาจารย์ที่ปรึกษา : ศาสตราจารย์ ดร. บุนยรัชต์ กิติยานันท์ และ ศาสตราจารย์ ดร. โรเบิร์ต เอ็ม ซิฟฟ์ 80 หน้า

แบบจำลองมอนติคาร์โลเชิงจลนพลศาสตร์ถูกนำมาใช้เพื่อศึกษาพฤติกรรมทางจลนพลศาสตร์ของการเกิดผลิตภัณฑ์คาร์บอนหนึ่งและสองอะตอมในปฏิกิริยาสังเคราะห์ฟิชเชอร์-โทรปช์บนตัวเร่งปฏิกิริยาโคบอลท์โดยการปรับสภาวะของปฏิกิริยา แบบจำลองของปฏิกิริยาซึ่งได้แก่ กลไกคาร์ไบด์และกลไกการแทรกสอดของคาร์บอนมอนอกไซด์ถูกนำมาประยุกต์ใช้ในการจำลองเพื่อคำนวณหาอัตราการเกิดผลิตภัณฑ์และสัดส่วนของสารที่ถูกดูดซับบนพื้นผิวตัวเร่งภายใต้สภาวะคงที่ นอกจากนี้ การทำงานร่วมกันของกลไกคาร์ไบด์และการแทรกสอดของคาร์บอนมอนอกไซด์ยังถูกใช้เพื่อแสดงให้เห็นถึงความเป็นไปได้ในการดำเนินของแต่ละกลไก และเปรียบเทียบผลลัพธ์ที่ได้กับผลการทดลองก่อนหน้านี้ที่สภาวะเดียวกัน จากการศึกษาพบว่าการสร้างพันธะระหว่างคาร์บอนส่วนใหญ่เกิดขึ้นโดยการแทรกสอดของคาร์บอนมอนอกไซด์บนพื้นผิวไปยังพันธะระหว่างโลหะกับเมธิล ซึ่งผลลัพธ์จากแบบจำลองตามกลไกการแทรกสอดของคาร์บอนมอนนอกไซด์แสดงให้เห็นว่าสภาวะของกระบวนการมีผลกระทบต่อความสามารถในการเกิดปฏิกิริยาและสัดส่วนของผลิตภัณฑ์เป็นอย่างมาก ระบบเกิดสภาวะไร้ปฏิกิริยาที่อุณหภูมิต่ำกว่า 463 เคลวิล และที่อัตราส่วนของไฮโดรเจนต่อคาร์บอนมอนอกไซด์ในสารตั้งต้นที่ถูกป้อนน้อยกว่า 1.1 สำหรับสภาวะคงที่ที่เกิดปฏิกิริยาได้ พื้นผิวของตัวเร่งปฏิกิริยาจะถูกปกคลุมด้วยอะตอมของไฮโดรเจนและโมเลกุลของคาร์บอนมอนอกไซด์ที่ถูกดูดซับเป็นส่วนใหญ่ ซึ่งมีบทบาทสำคัญในการเติบโตของสารไฮโดรคาร์บอนโซ่ตรง

GRAPHICAL ABSTRACT

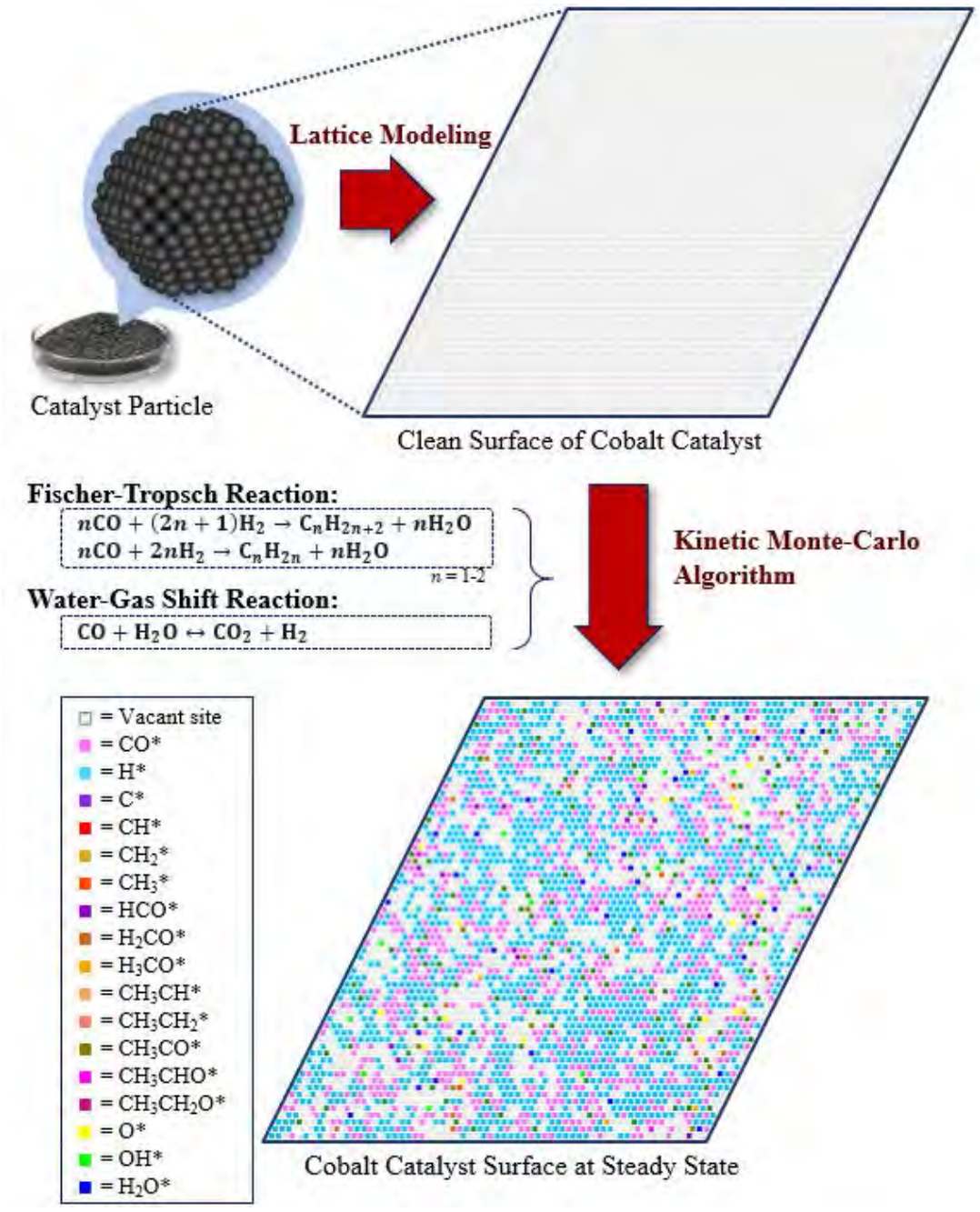

ACKNOWLEDGEMENTS

The author would first like to acknowledge the Petroleum and Petrochemical College, Chulalongkorn University. This accomplishment would not have been possible without many supports. The author would profoundly like to thank my thesis advisor Prof. Boonyarach Kitiyanan for consistently providing me from the beginning with the valuable advice of the researching and writing the thesis. He always suggests me about the process in my study and work, and in my life as well. The author would also like to thank my co-advisor Prof. Robert M. Ziff of the University of Michigan, for his professional suggestion to solve the trouble spot and achieve the research. In addition, the author would like to express my appreciation to my thesis committee Asst. prof. Kitipat Siemanond and Dr. Sitthiphong Pengpanich, for taking the time to review and comment on this thesis.

The author is grateful for the full scholarship and funding of this thesis work provided by the Petroleum and Petrochemical College, and the Petroleum and Petrochemical College and Center of Excellence on Petrochemical and Materials Technology.

The author would also like to acknowledge my seniors Mr. Palawat Unruean, Mr. Kumpanart Dechakumpoo and Mr. Sirawit Pruksawan, and to thank my friends for their precious assistance, suggestion and encouragement to work and improve the thesis.

Finally, the author must indispensably express my profound gratitude to my parents for providing me continuously with invaluable support and encouragement throughout my years of study and my life. Thank you all.

TABLE OF CONTENTS

LIST OF TABLES

TABLE **PAGE**

LIST OF FIGURES

FIGURE **PAGE**

FIGURE **PAGE**

FIGURE **PAGE**

FIGURE **PAGE**

CHAPTER I
INTRODUCTION

The Fischer-Tropsch synthesis is heterogeneous catalytic reaction to produce hydrocarbons from syngas (CO and H_2). The product distribution and selectivity of hydrocarbon products directly depend on the reaction pathways, which are related to the process conditions such as temperature, pressure and H_2/CO feed molar ratio, as examined in several experiments (Dry, 2002; Todic *et al*., 2014 and 2016; Lualdi *et al*., 2012; Mansouri *et al*., 2014; Kasht *et al*., 2015). Cobalt is the widely used metal to catalyze the Fischer-Tropsch reaction because of its high activity and stability. Moreover, cobalt has low activity for the Water Gas Shift reaction which is a side reaction occurring during Fischer-Tropsch reaction (Qiu *et al*., 2017). The kinetics of Fischer-Tropsch synthesis is believed to follow the Langmuir-Hinshelwood model. Two general mechanisms have been proposed to describe the hydrocarbon chain growth in the Fischer-Tropsch Synthesis, which are the carbide mechanism and the CO insertion mechanism. However, in spite of a large number of experimental researches, a correct reaction mechanisms of this reaction are still unclear and difficult to understand only through the experimental methods.

Kinetic Monte-Carlo (KMC) is a computer method that is widely used to investigate the catalytic reaction mechanisms and analyze the kinetics of the reaction. In the KMC simulation, the configuration of the catalyst surface on a molecular scale can continuously be evolved to reach the larger time scales by the processes in a small-time step, according to the probability of each process (Ustinov *et al*., 2019). This allows the KMC to link the processes on the atomic level and the macroscopic kinetics (Jansen, 2012). The KMC simulation has been used to study the catalytic reaction and present the state of the catalyst surface. The reactive and poisoned states occurring on the catalyst surface in the oxidation of CO have been indicated in the KMC simulation by Ziff, Gulari, and Barshad (called ZGB model) (Ziff *et al*., 1986). Furthermore, Tain *et al*. (2009) have also applied KMC for the Fischer-Tropsch synthesis to provide understandings of kinetic behavior on the surface of iron catalyst.

In this research, the KMC simulation was utilized to study the kinetic behavior of C_1 and C_2 formation in the Fischer-Tropsch synthesis over the cobalt catalyst

under the isothermal condition. Two reaction models, which are the carbide mechanism and the CO insertion mechanism, were simulated. Those two mechanisms were also combined to investigate the possibility of each reaction mechanism and compared the results with the reported experimental results at the same reaction conditions. The appropriate mechanism in this study was then suggested. Moreover, the effects of reaction temperature, pressure and H_2/CO molar ratio in feed were also evaluated.

CHAPTER II
LITERATURE REVIEW

2.1 Kinetic Monte-Carlo

Kinetic Monte-Carlo (KMC) simulation is one computational algorithms used to study the phenomena of heterogeneous catalyst in microscopic scale by numerically solving the master equation to predict the probability of process pathways occurred on surface. It provides a simple powerful and flexible tool to study about a relatively general approach for exploring the thermodynamic, kinetic behavior of fundamental arbitrary transitions sequences and reaction on the surface catalysts. Although the kinetics of surface reaction is generally described by the macroscopic rate equation, but the normal assumption for this equation is that the adsorbates are distributed randomly over the surface. In addition, the structure of the adlayer is impossible to illustrate by rate equation.

Three parts can be distinguished in a KMC method; the physical model representing catalyst surface and its occupation with adsorbates, the master equation describing the evolution of system, and the KMC algorithm solving the master equation to obtain the possible process pathways.

2.1.1 Physical Model

The actually important basis of surface reaction is the active sites, which atoms or molecules are adsorbed and activated to react with each other. To simulate the microkinetic model, the physical basis is necessary to determine the boundary where supports reactions or other processes taking place over catalyst surface. This can be called “physical model”. There are several aspects for physical models which are acceptable depending on the sequences of active sites.

2.1.1.1. Lattice-Gas Model

For the simple crystal surface, all active sites form a square grid or lattice. Therefore, the lattice can be used as the basis for modeling heterogeneously catalytic reactions with gas molecules in the KMC simulations. This one of phys-

ical models is called lattice-gas model. Each point located on each intersection represent for active sites called lattice points (Jansen, 2012). As shown in Figure 2.1, all of the lattice points correspond to positions of top sites on a (100) surface of a fcc metallic catalyst (dash-line circles correspond to metallic atoms).

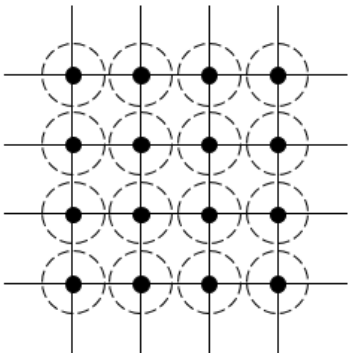

Figure 2.1 Lattice-gas medel used in KMC simulation

In addition, Jansen (2012) discussed the method indicating the positions of each lattice points for modeling the metallic catalyst surface. The concepts are locations of active sites in each unit cells and locations of unit cells on the surface. Therefrom, the positions of active sites on lattice model can be specified by expression 2.1.

$$\vec{s}^{(s)} + n_1\vec{a}_1 + n_2\vec{a}_2 \tag{2.1}$$

Where vector $\vec{s}^{(s)}$ correspond to position of site s or lattice point s in a unit cell $n_1\vec{a}_1 + n_2\vec{a}_2$. Where $n_1$and n_2 are integers corresponding to the order of unit cell in horizontal and vertical (n_1= n_2= 0 for the first unit cell), $\vec{a}_1$and $\vec{a}_2$ are primitive vectors which represent the horizontal and vertical axes. For the simple (100) surface of a fcc metallic catalyst which has just one top site per a unit cell, unit cell consists of vector $\vec{a}_1$= a(1,0) and vector $\vec{a}_2$= a(0,1) as shown in the bottom-left corner of Figure 2.2. Position of a top site in a unit cell is specified by vector $\vec{s}^{(0)}$= a(0,0). Thus, the position of a top site (black dot) located in the first unit cell is specified to $\vec{s}^{(s)} + n_1\vec{a}_1 + n_2\vec{a}_2$= a(0,0) + (0)·a(1,0) + (0)·a(0,1).

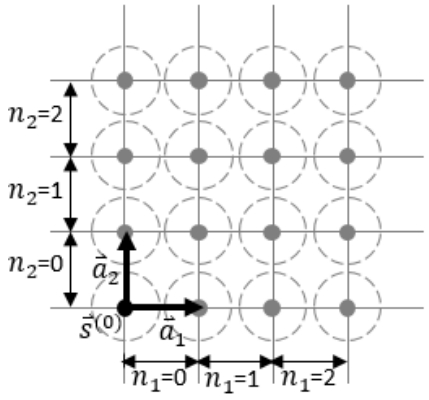

Figure 2.2 Indications of lattice points used in KMC simulation

However, a unit cell is possible to have more than one lattice point. The expression 2.1 can also be used to identify each point in this case. For the (111) surface of a fcc metallic catalyst, active sites form parallelogram lattice. In addition to top site, this surface is possible to consist of hcp hollow and fcc hollow sites. The lattice model for this case is shown in Figure 2.3. Its unit cell is specified by vector $\vec{a}_1$= a(1,0) and vector $\vec{a}_2$= a($\frac{1}{2}$, $\frac{\sqrt{3}}{2}$). A unit cell has three lattice point with $\vec{s}^{(0)}$= a(0,0) (top site represented by black dot), $\vec{s}^{(1)}$= a($\frac{1}{2}$, $\frac{\sqrt{3}}{6}$) (fcc hollow site represented by white dot), and $\vec{s}^{(2)}$= a(1, $\frac{\sqrt{3}}{3}$) (hcp hollow site represented by gray dot).

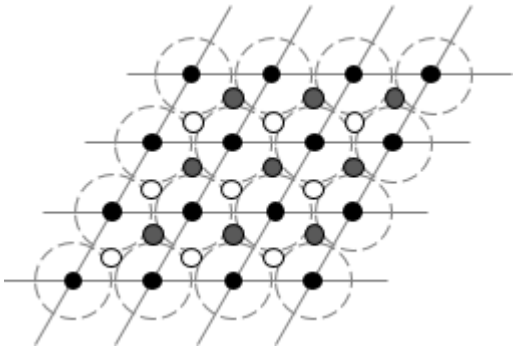

Figure 2.3 Parallelogram lattice including top, fcc hollow, and hcp hollow sites

2.1.1.2. Labels and Configurations

In order to model the surface reaction, positions of sites where adsorbates occupy and react with each other can be defined by expression 2.1. However, these sites must be identified that they are occupied or not, and occupied sites with which adsorbated species. This property, especially the occupation of the site, can be achieved by defining the label. The label is introduced to identify each lattice point where corresponds to the active site. For a site located at position $\vec{s}^{(s)} + n_1\vec{a}_1 + n_2\vec{a}_2$, The label can be defined by expression 2.2.

$$(n_1, n_2/i: site\ property) \tag{2.2}$$

For the clean surface, all sites behave as vacant sites which are not occupied by any molecules. The site property in expression above should be defined to be vacant sites which is represented by "$*$". Thus, labeling for vacant site located at lattice point i in any unit cell is $(n_1, n_2/i: *)$. Furthermore, labelling of all lattice points appeared on a lattice together called "configuration" which represent to occupation of entire substrate. The Figure 2.4 illustrates a configuration of (100) clean surface of fcc catalyst.

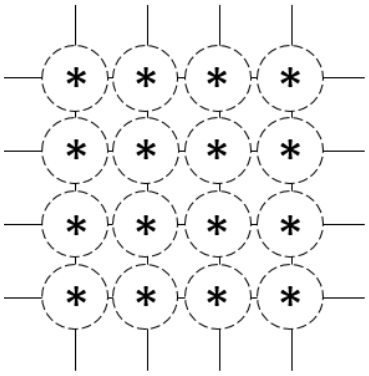

Figure 2.4 Configuration of clean surface with only vacant sites

The configurations corresponding to adlayer can be changed by processes occurred on substrate (i.e., adsorption, reaction, diffusion, etc.). These processes are also specified by labeling. The change of occupation in site i can be labeled by expression below.

$$(n_1, n_2/i: initial\ site\ occupation \rightarrow terminal\ site\ occupation) \tag{2.3}$$

For associative adsorption of a gas molecule A, molecule need to occupy on one vacant site. This case lead to change a label of a lattice point which also changes the configuration. Labeling this process can be achieved by (n_1, $n_2/0$:$*\rightarrow A$). The change of configuration is shown in Figure 2.5 which exhibits before and after associative adsorption of A into a vacant site i located in n_1-n_2 unit cell.

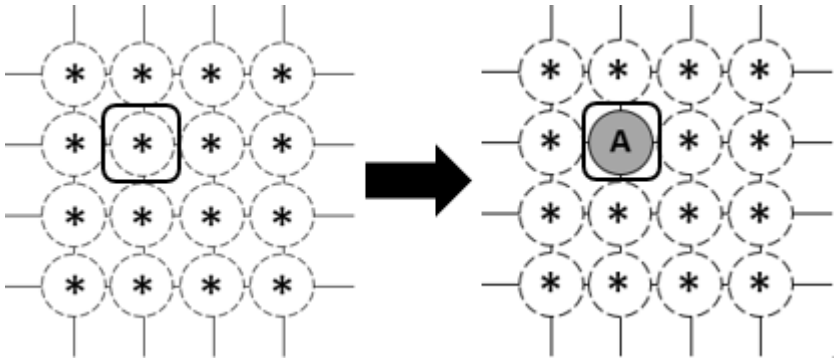

Figure 2.5 Configuration changing with associative adsorption of a molecule A

The dissociative adsorption is similar to associative adsorption, but it need two adjacent sites for occupying. For dissociative adsorption of molecule B_2 as shown in Figure 2.6, two points must be specified. Labeling this process can be achieved by $\{(n_1, n_2/0), (n_1{+}1, n_2/0) : **\rightarrow BB\}$.

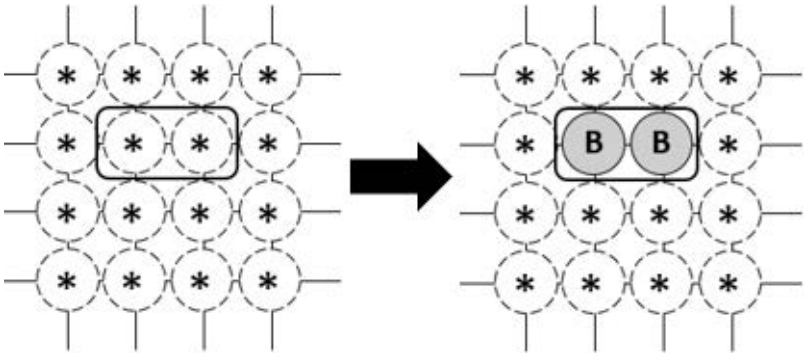

Figure 2.6 Configuration changing with dissociative adsorption of a molecule B_2

The adsorbate A (Figure 2.5) can hop to another neighboring site. If molecule hop to the right of original site. This process can be labeled by $\{(n_1, n_2/0), (n_1{+}1, n_2/0) : A *\rightarrow * A\}$ as shown in Figure 2.7.

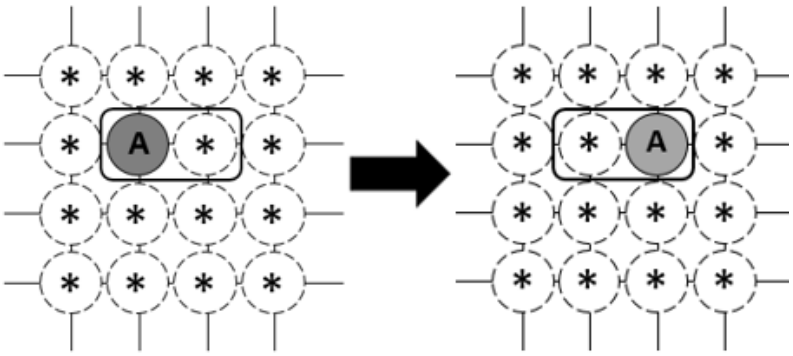

Figure 2.7 Configuration changing with diffusion of a molecule A

If adsorbated A can react with adsorbated B occupied on neighboring site and desorb immediately product, two occupied sites will change to two vacant sites as labeled by $\{(n_1, n_2/0), (n_1{+}1, n_2/0) : AB \rightarrow **\}$. This process is shown by Figure 2.8.

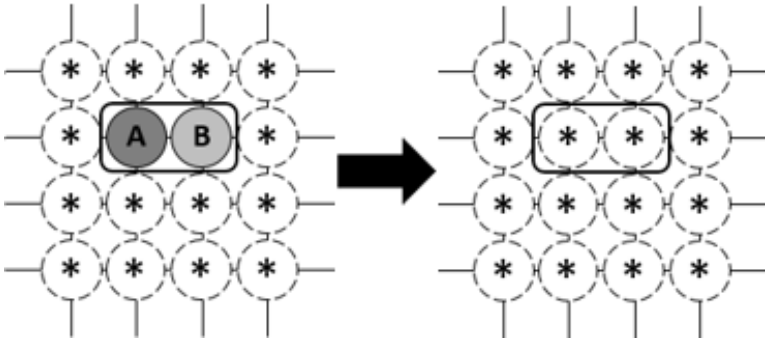

Figure 2.8 Configuration changing with reaction of adsorbated A and B

2.1.2 Master Equation

The master equation is the most important equation used in KMC method which describes how probabilities of appeared configurations change in time. It corresponds to the evolution of adlayer or substrate. The general form of master equation is shown in equation 2.4 (Jansen, 2012).

$$\frac{dP_\alpha}{dt} = \sum_\beta [W_{\alpha\beta} P_\beta - W_{\beta\alpha} P_\alpha] \tag{2.4}$$

Where α and β refer to configurations of adlayer or substrate, P_α and P_β are their probabilities, $W_{\alpha\beta}$ and $W_{\beta\alpha}$ are transition probabilities per unit time which specify the rate for adlayer or substrate change due to processes occurred on substrate, and t is time. The first term on the right-hand side represent to the increases of P_α due to processes changing from other configurations β to α. On the other hand, the second term represent to the decreases of P_α due to processes changing from configurations α to the others. To study kinetics of surface reactions with KMC method, the master equation is regarded as center equation which obtains the transition probabilities from quantum chemical method and is solved by KMC algorithm for obtaining results, as shown in Figure 2.9.

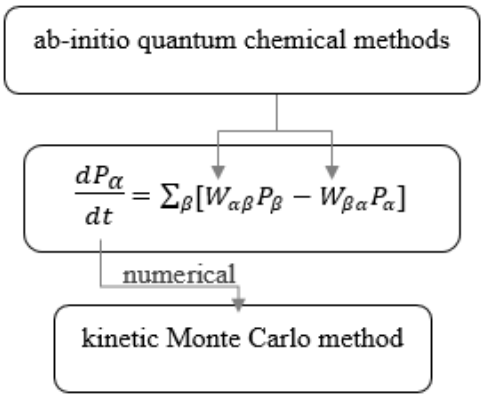

Figure 2.9 Processes simulating kinetics of surface reactions with KMC

In the kinetics, the transition probabilities can be regarded as kinetic rate constants which change the occupations of the sites by reactions or other processes. Simulating microkinetic models, individual rate constants of elementary steps correspond to the change in configurations of adlayers.

In the case of reaction, rate constant k_i of elementary reaction i can be calculated by Arrhenius equation, where A_i is pre-exponential factor, Ea_i is activation energy, R is universal gas constant, and T is temperature.

$$k_i = A_i \exp\left(\frac{-Ea_i}{RT}\right) \tag{2.5}$$

The parameters Ea_i and A_i can be evaluated by the Density-Functional Theory (DFT) calculation which correspond to motions of molecules in quantum mechanical.

In the case of adsorption, rate constants are dependent on partial pressure of reactants in gas phase. Rate constant of adsorption can be calculated by

$$k_i = S_i J_i P_x \quad (2.6),$$

where S_i is sticking coefficient, J_i is impinging constant, and P_x is partial pressure of reactant species x.

2.1.3 Kinetic Monte-Carlo Algorithms

The KMC algorithms statistically generate a sequence of configurations related to time that the transitions between these configurations occur by numerically solving the master equation to predict the probability of process pathways. Simulation produces an ordered set of configurations and times when processes occur as shown in expression below.

$$(\alpha_0, t_0) \xrightarrow{\Delta t_1} \alpha_1 \xrightarrow{\Delta t_2} \alpha_2 \xrightarrow{\Delta t_3} \alpha_3 \xrightarrow{\Delta t_4} \ldots \quad (2.7)$$

This series of transitions from a configuration to another is called Markov chain, where α_0 and t_0 are initial configuration and time of simulation. The changes of configurations ($\alpha_{n-1} \rightarrow \alpha_n$) called Markov changes are caused by reactions or other processes (Santen, 2015). The probability that the master equation describe that the system is still in the present configuration α_n at a later time t_{n+1} is given by $\exp[-\sum_\beta W_{\beta\alpha}\,(t_{n+1} - t_n)]$, where $\sum_\beta W_{\beta\alpha}$ represents to total transition probabilities. Therefore, the time interval Δt when no process occurs until there is next process is calculated by

$$\Delta t = -\frac{1}{\sum_\beta W_{\beta\alpha}} \ln(r) \quad (2.8),$$

here r is a uniform deviate on the unit interval.

There are many algorithms that yield the sequence of configurations. They are all equivalent that all need to repeatedly determine the time that next process will occur, the type of process that will occur, and the position on surface that process will occur. The general algorithms used in kinetic surface reaction include Variable Step Size Method (VSSM), Random Selection Method (RSM) and First Reaction Method (FRM).

2.1.3.1. Variable Step Size Method

To produce KMC algorithms, the determination of all processes that are possible taking place in system and their rate constants is required to provide the process pathway that generate the sequence of configuration. A popular one of KMC algorithm is the Variable Step Size Method (VSSM). It is a simple method that can be made very efficient.

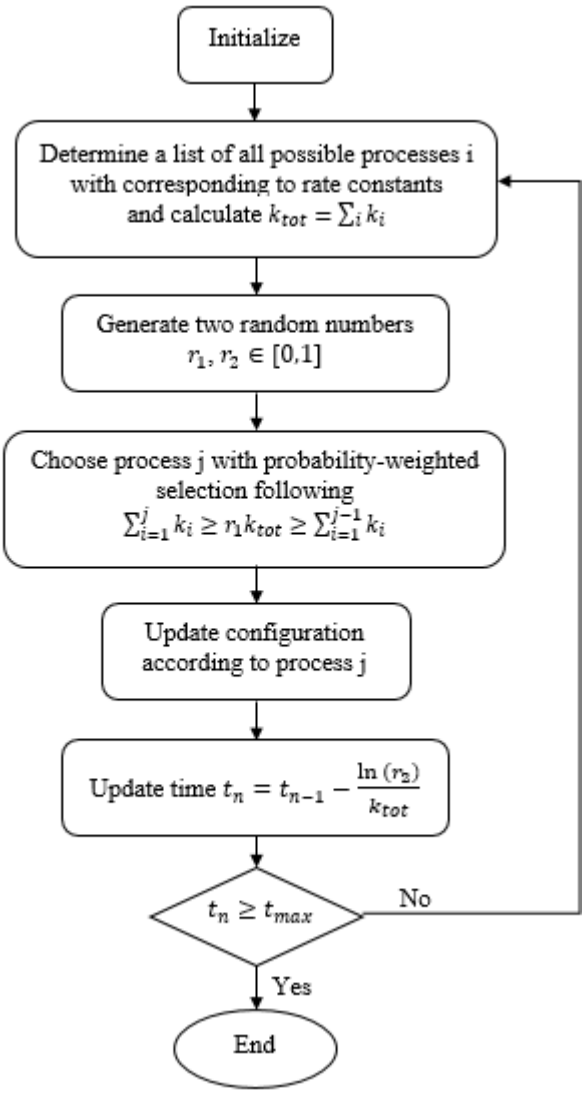

Figure 2.10 VSSM algorithm

The algorithm of VSSM is shown in Figure 2.10. It is initialized by generating an initial configuration α_0 (mostly as clean surface with whole vacant sites) and setting initial time (mostly as t_0). Then, a list all possible processes or evens i with corresponding to rate constants need to be determined and calculate the total rate constant of all processes ($k_{tot} = \sum_i k_i$). The transition of configuration is caused by a selected process j from all possible processes which fulfills the condition

$$\sum_{i=1}^{j} k_i \geq r_1 k_{tot} \geq \sum_{i=1}^{j-1} k_i \quad (2.9),$$

where $r_1 \in [0,1]$ is uniformly distributed random number. This method used to choose a process j is called probability-weighted selection. For the concept of this method as shown in Figure 2.11 where the widths of the blocks correspond to values of rate constants. The higher rate constant tends to be more selective.

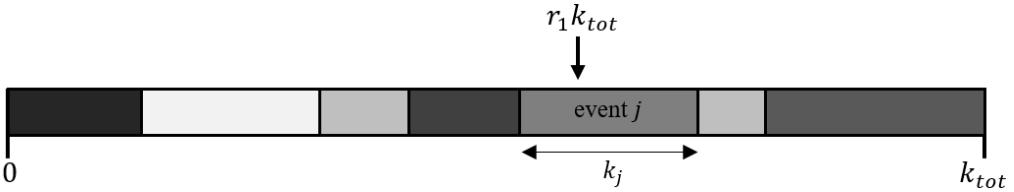

Figure 2.11 Scheme illustrated probability-weighted selection method

To execute the selected process, the configuration is changed to new one, and system time is advanced by equation (2.10).

$$t_n = t_{n-1} - \frac{\ln(r_2)}{k_{tot}} \quad (2.10)$$

The $r_2 \in [0,1]$ is another random number. If the system time t_n is less than the total simulated time, then in back to update a list of all possible process, otherwise, it stops.

2.1.3.2. Random Selection Method

Although the VSSM is very efficient surface simulations, but it need to determine the process type that is possible to take place at location of process and need to update a list of all possible process at every transition. Hence, VSSM involves quite a bit of bookkeeping that require the large computational memory scale. Instead of determinations of processes depended on locations, it is possible to split in these two parts independently by Random Selection Method (RSM).

The algorithm of RSM is shown in Figure 2.12, which generates type of processes, process times and location of process independently. The probabilities that individual processes occur are determined by $p_i = k_i/k_{tot}$ which are used to accept processes in probability-weighted selection. To change the configuration, the type as well as the location of process are chosen randomly. Terminally, only configuration and time of system need to be updated.

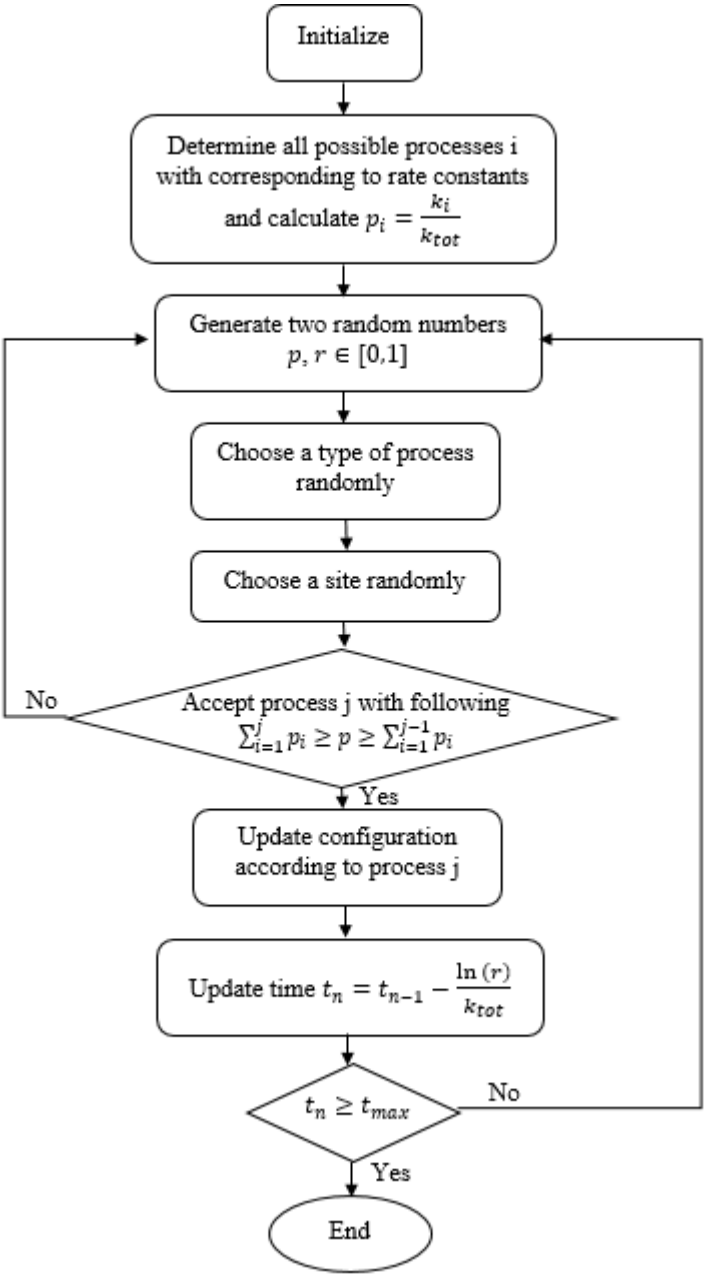

Figure 2.12 RSM algorithm

2.1.3.3. First Reaction Method

Instead of calculating three parts (type, location and time of process) independently, the First Reaction Method (FRM) prefer to combine all three parts. It can be done by making a list of all possible processes and generating a time occurrence for each process $\alpha \rightarrow \beta$ by

$$t_{\beta\alpha} = t_{\alpha} - \frac{\ln(r)}{W_{\beta\alpha}} \quad (2.11),$$

where $W_{\beta\alpha}$ is rate constant for process $\alpha \rightarrow \beta$, and $r \in [0,1]$ is uniformly distributed random number. This process time is used for choosing the process with probability-weighted selection that the process with the shortest time tends to be more selective. Therefore, the selected process always relates to process time and location.

2.1.3.4. Practical Consideration

The efficiency of methods extremely depends on details of algorithm. In addition to the accuracy, very important points that should be regarded in computer simulations are memory scale and computer operating time. These are mainly caused by data structures that are used in algorithms which involve the calculation of process types and process location. Excepting time steps, they use a little computer time to calculate.

The combination of all three parts consisted of the process types, process times, and process sites is introduced in FRM. The selections of processes actually relate to the sites where each process can take place and the times when process takes place. These operations involve a lot of bookkeeping that require the large computational memory scale. Thus, FRM may not be good choice for a large system. The VSSM is generally the best method to use unless the number of process types is large. It prefers to determine the process types that are possible to take place at related sites although they are independent to process times. Therefore, it involves quite a bit bookkeeping. The RSM should be considered if processes in the system can occur almost everywhere.

Table 2.1 Number of processes simulated per second for ZGB model

	Types of methods		
	VSSM	RSM	FRM
Number of processes simulated per second	1900	3200	940

Jansen (2012) simplified the comparison of these three methods by using Carlos program. Different models of surface reaction are evaluated for resulting just number of processes simulated per second. The Ziff-Gulari-Barshad (ZGB) model, surface simulation of CO oxidation (more detail is described in literature Ziff *et al*., (1986)), is also evaluated. Table 2.1 shows that the RSM is the most efficient with lowest computer operating time. Thus, it is chosen to simulate surface reaction in present study.

2.1.4 Literature Reviews

Ziff *et al*. (1986) introduced the simulation to study the kinetic phase transitions in the surface reaction of CO oxidation called Ziff–Gulari–Barshad (ZGB) model. The reaction model, based on the Langmuir-Hinshelwood (LH) mechanism, is simplified to three elementary reactions. There are associative adsorption of CO, dissociative adsorption of O_2, and formation of CO_2 with an O located on neighboring site of a CO adsorbate and desorption of CO_2 immediately. The probabilities of each elementary depend on composition of CO in gas phase (y_{CO}).

The simulation starts with the random collision of gas molecule on active sites contained in square lattice. The probability for choosing CO to be colliding molecule is y_{CO} and for choosing O_2 to be colliding molecule is $1\text{-}y_{CO}$. After the colliding molecule is chosen, a site on lattice will be randomly chosen for occupation of this molecule. If this site is already occupied, this adsorption is refused to occur. When colliding molecule can occupy on site, the neighboring sites are checked. If one or more neighboring sites are already occupied by another adsorbate species, change both sites to be two vacant again.

The steady-state configuration is produced by ZGB simulation as shown in Figure 2.13 which starts with clean lattice of 128x256 sites (represented by

black dot) and y_{CO} = 0.5. It shows that O atoms (represented by white dot) mostly occupy on sites. However, there are few CO clusters (represented by gray dot) remaining on surface. Because CO molecules in clusters can not meet O at neighboring.

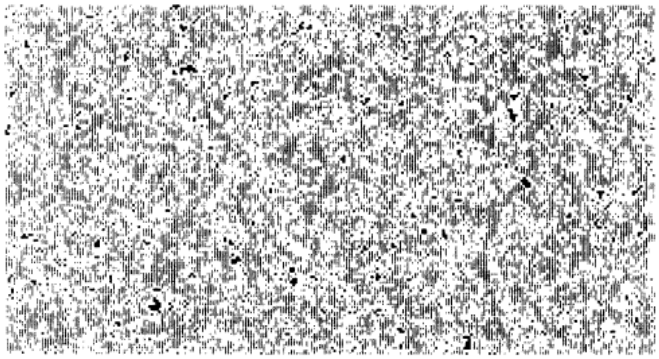

Figure 2.13 Snapshot of CO oxidation on surface under steady state produced by ZGB model (Ziff *et al*., 1986)

In addition, the result of y_{CO} variation show that the transition state or reaction can only occur in range of y_{CO} between critical values y_1 ($y_1 = 0.389 \pm 0.005$) and y_2 ($y_2 = 0.525 \pm 0.001$). For y_{CO} above y_2, the surface is completely covered by adsorbated CO, which is called adsorbing state of CO or CO poisoning state. On the other hand, the system evolves into O poisoning state with y_{CO} below y_1. There is also no reaction occur. As shown in Figure 2.14, the surface is covered by both CO and O with the value of y_{CO} between y_1 and y_2, leaded to production of CO_2. This state is called the phase transition state.

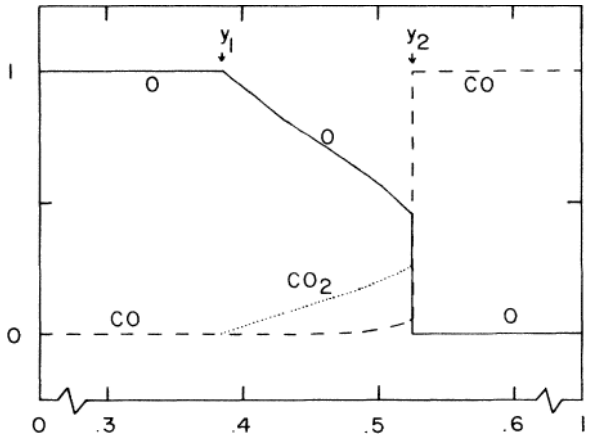

Figure 2.14 Average coverage fractions of CO, O and CO_2 as function of y_{CO} (Ziff *et al.*, 1986)

Pruksawan *et al*. (2016) developed the KMC simulation to study kinetic behavior in partial oxidation of CH_4 over a nickel based on LH mechanism. Hence, this available simulation can be used to optimize the operating conditions included feed concentration of CH_4 (y_{CH4}) and reaction temperature to maximize production rate of CO_2. Moreover, the effects of diffusion of adsorbed species and inactive impurities on surface are also evaluated. The reaction model mainly consists of associative adsorption of CH_4 and dissociative adsorption of O_2 on adsorption sites, formations of H_2, H_2O, CO and CO_2, and desorption of products. The information of kinetic parameters are obtained from experiments and inputted to simulation. The simulation results are acceptable and agreeable with experimental studies. Hence, the simulation is available to be used as optimizing tool. In addition, the results indicate that the phase transition state occurs only for $y_1 < y_{CH4} < y_2$, where $y_1 = 0.47 \pm 0.01$ and $y_2 = 0.71 \pm 0.01$. The y_{CH4} of 0.65 and the temperature of 850 K yield the maximum production rate of CO_2.

Hess and Over (2013) created DFT-based KMC simulation in order to understand the reaction mechanism and reactivity of $RuO_2(110)$ in the Deacon reaction that describes the oxidation of HCl with O_2 yielding Cl_2 and H_2O. Although the Deacon reaction over RuO_2 can be investigated by the ultra-high vacuum (UHV) experiments, but detailed microscopic catalyst properties are still lack. For this reason, the computational simulations of surface reactions are introduced. DFT calculations were

used to determine lateral interaction and hydrogen bond energies that are required parameters in KMC simulations. The KMC simulations were finally used to describe details of surface processes that can involve the long-term blocking of sites due to trapping of reactants that reduces active catalyst surface.

Piccinin *et al*. (2014) used the KMC simulation to understand the kinetic behavior of CO oxidation on Pd(111) surface. The DFT method is used to provide the kinetic parameter for KMC simulation. The model for Pd(111) is considered as containing with two types of active sites, fcc and hcp hollow site. The two-dimensional square lattice of 96×96 sites used in study with the assumption of periodic boundary conditions and no segregation in two types of sites. However, fcc and hcp sites are labeled with difference shape, circle for fcc and triangle for hcp. Figure 2.15 illustrates the snapshot from KMC at high coverage including 0.44 ML of CO (blue color) and 0.18 of O (red color).

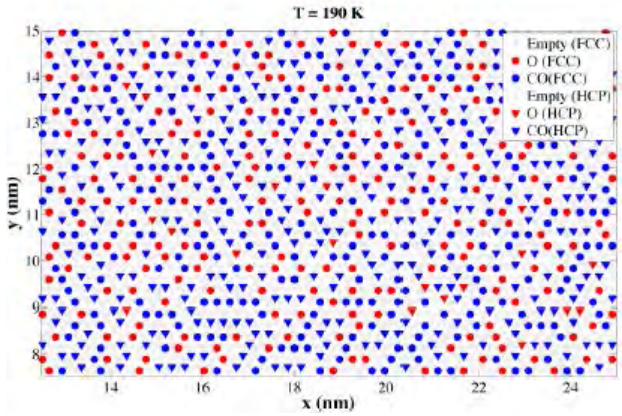

Figure 2.15 Snapshot the lattice with 0.44 ML of CO coverage and 0.18 ML of O coverage (Piccinin *et al*., 2014)

2.2 Fischer-Tropsch Synthesis over Cobalt Catalyst

Fischer-Tropsch Synthesis is one important reaction in petroleum industries. This reaction converts a mixture of CO and H_2 into various hydrocarbon fuels with the presence of metal catalysts such as Co, Fe, Ru, etc. Fischer-Tropsch synthesis was first developed in Germany by Franz Fischer and Hans Tropsch, in 1920s. It is operated in

typical temperature of 150 to 300 °C and pressure of 1 to several ten atmospheres. The higher temperature leads to higher reaction rate and higher conversion, but it also tends to favor methane production (Dry, 2002).

The Fischer-Tropsch synthesis involves a large series of reactions that produce a variety of hydrocarbon fuels. To produce normal paraffins (C_nH_{2n+2}) which are one of main products with a mixture of CO and H_2, Fischer-Tropsch synthesis proceeds via equation 2.12 where n is number of carbons forming straight chains.

$$nCO + (2n + 1)H_2 \rightarrow C_nH_{2n+2} + nH_2O \quad (2.12)$$

Other main products are olefins (C_nH_{2n}) that carbons form straight chain with the presence of double bonds. The productions of alkenes are proceeded by Fischer-Tropsch synthesis via equation below where n is more than one.

$$nCO + (2n)H_2 \rightarrow C_nH_{2n} + nH_2O \quad (2.13)$$

The possible by-product is CO_2 that is formed by the water-gas shift (WGS) reaction. It consumes the reactant CO with the presence of stream to produce CO_2 and H_2 as follows:

$$CO + H_2O \rightarrow CO_2 + H_2 \quad (2.14).$$

All above reactions occur on the catalyst surfaces. First, catalysts adsorb reactant molecules in gas phase. After that, they activate reactants located in adjacent sites to react each other if they are possible. The transition metal of Ru, Fe and Co are highly effective to convert syngas consisting of CO and H_2 into hydrocarbon fuels. Although Ru-based Fischer-Tropsch synthesis catalysts have high activity and high selectivity, but they are not suitable for commercial use due to their scarcities. Fe-based catalysts are low stability compared to Co. In addition, Co-based catalysts should be more suitable with the reasons of higher stability, lower cost, and lower CO_2 emission (Qui *et al*., 2017).

2.2.1 Co-based Fischer-Tropsch synthesis Catalysts

The Co-based catalysts are widely used in commercial Fischer-Tropsch synthesis processes. They give high stability as well as low activity for WGS reaction that produces CO_2. The Fischer-Tropsch synthesis using Co as catalyst yields mainly paraffins and few olefins.

Chen *et al.* (2017) distinguished Co into two crystallographic phases including hexagonal close-packed (hcp) phase and face-centered cubic (fcc) phase. The differences between hcp and fcc Co are bulk symmetries and atomic packing sequences that affect to the variety of exposed facets. Thus, the activity and selectivity of these two phases are different.

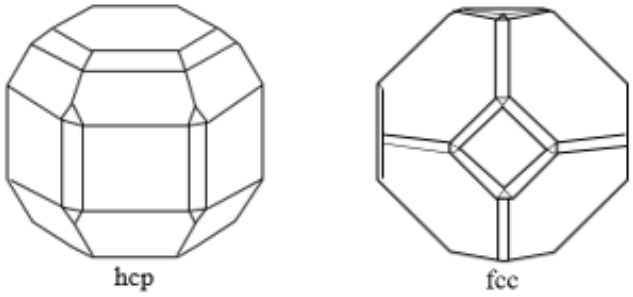

Figure 2.16 The hcp Co (left) and the fcc Co (right)

Lui *et al.* (2013) shew the shapes of hcp and fcc phases of Co as shown in Figure 2.16. The hcp has a dihedral shape, and the fcc has an octahedral shape. In addition, the comparison of activity between these two Co phase was investigated exhibiting that the hcp Co is more active than the fcc. Therefore, the hcp phase yields significantly higher reaction rates in Fischer-Tropsch synthesis. This is reasonable considering the hcp phase used as Co-based catalysts.

2.2.2 Fischer-Tropsch synthesis Reaction Mechanism

The Fischer-Tropsch synthesis can be considered as a polymerization reaction. The growth of the hydrocarbon chains leads to variety of products. The heterogeneous catalytic Fischer-Tropsch synthesis reaction starts with the adsorption of syngas reactants including CO and H_2 on the surface-active sites. The CO molecules are molecularly adsorbed on one vacant sites, becoming CO* species. These adsorbates are necessary to be cleaved into started carbon species for chain growth mechanism. Finally, the longer-chain hydrocarbons will be removed from the sites leading to the old vacant sites.

2.2.2.1. Adsorption of syngas on Co-based catalysts

The preliminary step in heterogeneous catalytic reaction of Fischer-Tropsch synthesis is adsorption of syngas, a mixture of CO and H_2, on the adsorption sites. The adsorption sites of Co-based catalysts are possible to be separated in four types as shown in Figure 2.17. There are top sites located on the top of metal atom, bridge sites located between two metal atoms, and two types of hollow sites, face-centered cubic (fcc) and hexagonal-close packed (hcp), located between three metal atoms (Gunasooriya *et al*., 2015).

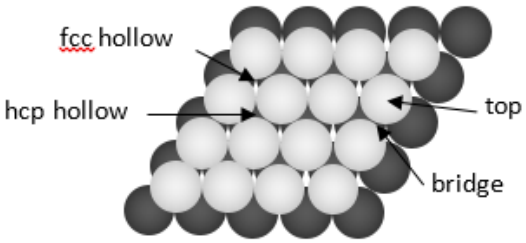

Figure 2.17 Active sites types

The Fischer-Tropsch synthesis reaction are mostly proposed that it proceeds via the basis of the Langmuir-Hinshelwood (LH) mechanism (Yang *et al*., 2013). Based on LH mechanism, reactants both CO and H_2 are adsorbed in order to take place reactions on the catalyst surface. The CO molecules are adsorbed molecularly into a vacant site ($CO + * \rightarrow CO^*$) and the H_2 molecules are dissociatively adsorbed into two vacant sites ($H_2 + 2* \rightarrow 2H^*$).

2.2.2.2. Dissociation of CO and Chain-Growth Reaction

The C-O bond cleavage in adsorbated CO is one of the key steps in Fischer-Tropsch synthesis mechanism. The dissociation of CO provides C_1 species containing one carbon atom that initiates chain-growth mechanism. After the adsorption of CO, this adsorbed CO can directly dissociate into a C* species following $CO^* \rightarrow C^* + O^*$ (Li *et al*., 2012). In addition to direct dissociation of CO, the C-O bond scission can occur though hydrogen assisting which is called “H-assisted dissociation”. In this case, one hydrogen atom occupying on a site is added to adsorbated CO to produce CHO intermediate converting into either C* + OH* or CH* + O*

(Shetty *et al*., 2009). Qi *et al*. (2014) studied the kinetics in Fischer-Tropsch synthesis mechanism including the direct dissociation and the H-assisted dissociation of CO by using DFT. The result shows that the H-assisted CO dissociation is more favorable to occur on Co(0001) surface due to lower activation barrier.

Santen *et al*. (2013) introduced two dominant mechanisms of Fischer-Tropsch synthesis reaction including carbide mechanism, the original mechanism proposed by Fischer and Tropsch, and CO insertion mechanism proposed by Pichler and Schultz. Figure 2.18 illustrate the Fischer-Tropsch synthesis reaction scheme according to carbide mechanism. The chain growth of adsorbated hydrocarbon intermediates (C_nH_y) in carbide mechanism proceeds via stepwise insertion of CH_x species which are formed by C_1 generated from CO dissociation and are acceptable considering as monomer. The hydrogenation of these adsorbated hydrocarbon chains then lead to the production of alkanes, and the dehydrogenation then lead to the production of double bonds in alkenes. Finally, adsorbed products are all removed from the surface into gas phase immediately.

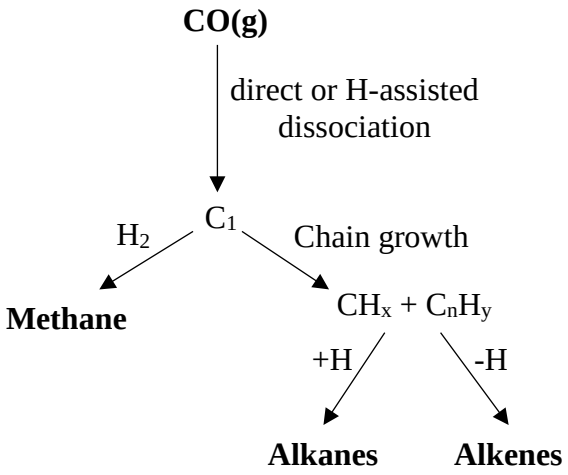

Figure 2.18 Reaction scheme of Fischer-Tropsch synthesis based on carbide mechanism adapted from Santen *et al*.

In addition to the original carbide mechanism, Fischer-Tropsch synthesis mechanism producing paraffins and olefins can proceed though CO insertion mechanism as shown in Figure 2.19. Instead of CH_x, the adsorbated hydrocar-

bon intermediates are inserted by CO converting to adsorbated oxygenate intermediates (C_nH_yCO). However, the hydrocarbon chain growth of oxygenate still occurs with CH_x monomer. After the production of longer oxygenates with various number of carbons, these long-chain oxygenates will be dehydroxylated in order to remove oxygen from hydrocarbon chains. Similar to the termination in carbide mechanism, the hydrogenation of adsorbated hydrocarbon chains leads to the production of alkanes and the dehydrogenation then lead to the production of alkenes.

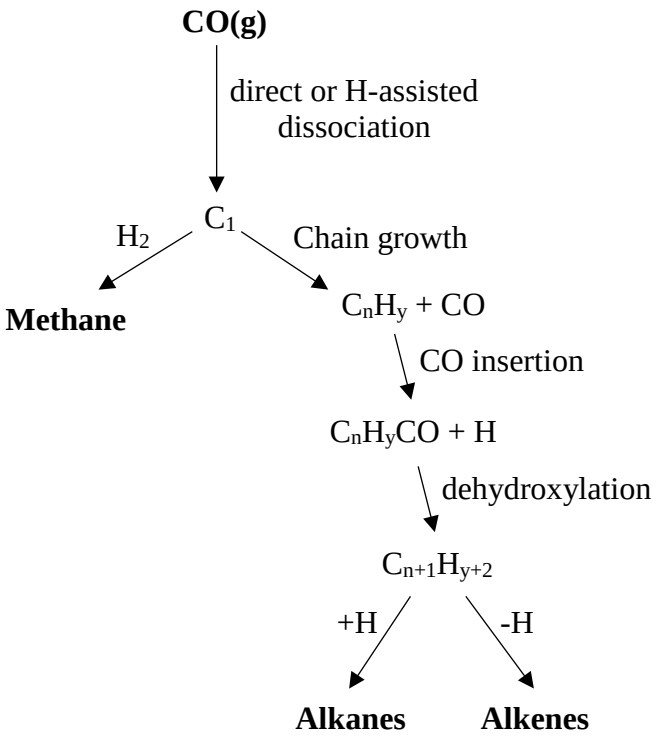

Figure 2.19 Reaction scheme of Fischer-Tropsch synthesis based on CO insertion mechanism adapted from Santen *et al*.

Storsæter *et al*. (2006) determined elementary reactions in Fischer-Tropsch synthesis producing paraffin and olefin products up to C_2 over Co-based catalysts in order to calculate their activation energies and pre-exponential factors. The formations of CO_2 and H_2 in WGS reaction are also involved. The elementary steps for formation of hydrocarbon base on both carbide mechanism and CO insertion mechanism. Figure 2.20 illustrates the carbide mechanism for formation of hydrocarbon products including methane, ethane, and ethylene. First, the adsorption of CO over

surface and H-assisted dissociation of CO* are introduced to provide C* and OH* species. The methane can be formed by stepwise hydrogenation of C* → CH* → CH_2* → CH_3* and finally CH_4. C_2H_6 and C_2H_4 are formed by reaction of CH_2* and CH_3*.

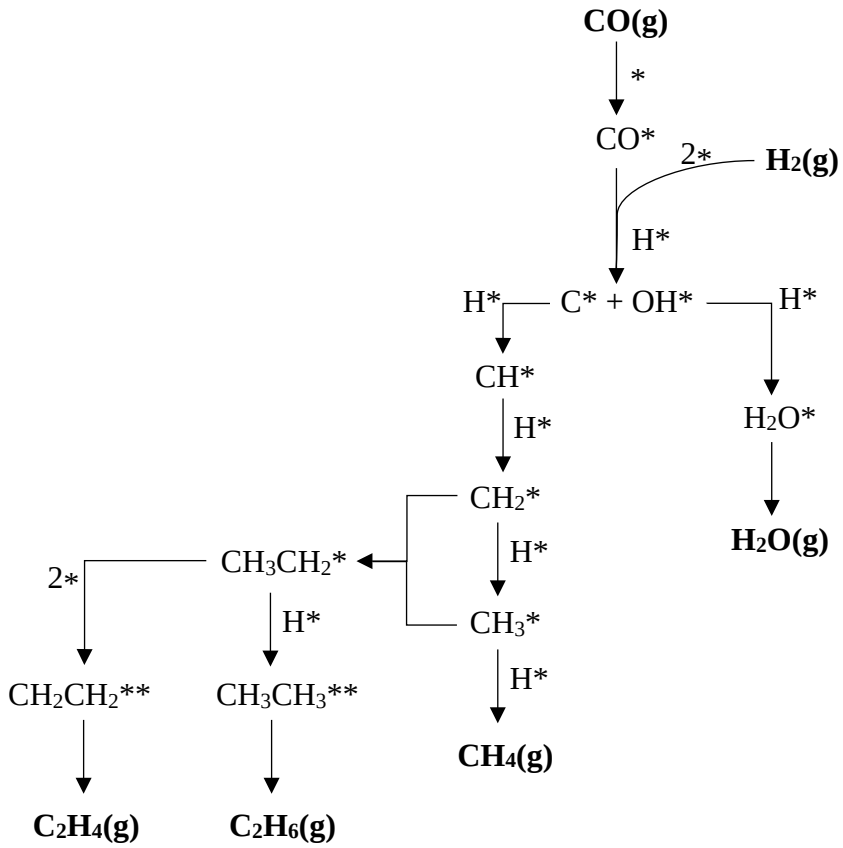

Figure 2.20 Reaction paths in Fischer-Tropsch synthesis based on carbide mechanism producing C_1-C_2 paraffins and olefins suggested by Storsæter *et al*.

In addition to the carbide mechanism, C_1-C_2 hydrocarbons can also be formed with CO insertion mechanism as shown in Figure 2.21. First, the adsorption of CO over surface and non-dissociative hydrogenation of CO* produce CHO* species which are stepwise hydrogenated following CHO* → CH_2O* → CH_3O*. The formed CH_3O* species are then dissociated directly into CH_3* which is hydrogenated into methane. Furthermore, insertion of CO* or CH_2O* into CH_3* yields C_2 products (C_2H_6 and C_2H_4). The WGS reaction producing CO_2 is another possible reaction involved in Fischer-Tropsch synthesis. The reaction paths for WGS are shown in Figure 2.22. The dissociation of adsorbed H_2O can directly occur to form H* and O*. This O* species finally react with adsorbed CO to form CO_2 products.

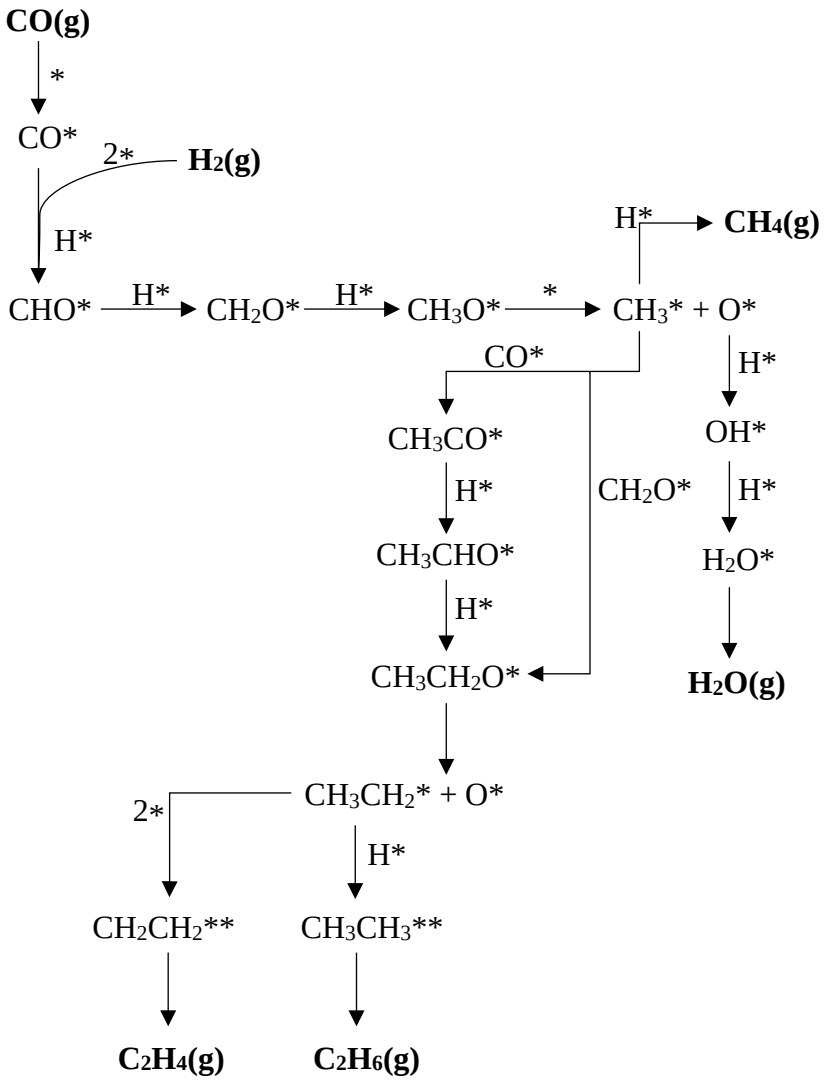

Figure 2.21 Reaction paths in Fischer-Tropsch synthesis based on CO insertion mechanism producing C_1-C_2 paraffins and olefins suggested by Storsæter *et al*.

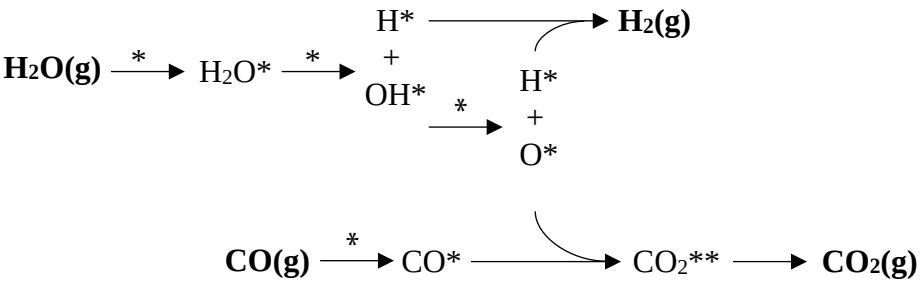

Figure 2.22 Reaction paths in WGS producing CO_2 and H_2

Based on all above reaction paths, Storsæter introduced all elementary reactions in Fischer-Tropsch synthesis containing 26 steps as shown in Table

2.2. The kinetic parameters for individual elementary reactions are calculated to establish the microkinetic model indicating that the conversion of CO is a good agreement with experimental results.

Table 2.2 All elementary steps in Fischer-Tropsch synthesis suggested by Storsæter *et al*.

Step	Elementary reaction	Step	Elementary reaction
1	$CO(g) + * \leftrightarrow CO*$	**14**	$O* + H* \leftrightarrow OH* + *$
2	$H_2 + 2* \leftrightarrow 2H*$	**15**	$CO* + O* \leftrightarrow CO_2**$
3	$CO* + H* \leftrightarrow C* + OH*$	**16**	$CO_2** \leftrightarrow CO_2(g) + 2*$
4	$C* + H* \leftrightarrow CH* + *$	**17**	$CH_3* + CH_2* \leftrightarrow CH_3CH_2* + *$
5	$CH* + H* \leftrightarrow CH_2* + *$	**18**	$CH_3* + CH_2O* \leftrightarrow CH_3CH_2O* + *$
6	$CH_2* + H* \leftrightarrow CH_3* + *$	**19**	$CH_3* + CO* \leftrightarrow CH_3CO* + *$
7	$CH_3* + H* \leftrightarrow CH_4(g) + 2*$	**20**	$CH_3CO* + H* \leftrightarrow CH_3CHO* + *$
8	$OH* + H* \leftrightarrow H_2O* + *$	**21**	$CH_3CHO* + H* \leftrightarrow CH_3CH_2O* + *$
9	$H_2O* \leftrightarrow H_2O(g) + *$	**22**	$CH_3CH_2O* + * \leftrightarrow CH_3CH_2* + O*$
10	$CO* + H* \leftrightarrow CHO* + *$	**23**	$CH_3CH_2* + H* \leftrightarrow CH_3CH_3**$
11	$CHO* + H* \leftrightarrow CH_2O* + *$	**24**	$CH_3CH_2* + 2* \leftrightarrow CH_2CH_2** + H*$
12	$CH_2O* + H* \leftrightarrow CH_3O* + *$	**25**	$CH_3CH_3** \leftrightarrow C_2H_6(g) + 2*$
13	$CH_3O* + H* \leftrightarrow CH_3* + O*$	**26**	$CH_2CH_2** \leftrightarrow C_2H_4(g) + 2*$

Furthermore, Asiaee *et al*. (2017) used the 26-step of existing elementary reactions suggested by Storsæter *et al*. to model the kinetics and the thermodynamics of Fischer-Tropsch synthesis elementary steps on a flat Co catalyst surface. The original mechanisms are a little bit adjusted. The activation barriers and reaction energies for individual steps resulted from modeling are compared to other theoretical studies. The comparison shows that the investigated energies are acceptable. This reason can support that this Fischer-Tropsch synthesis mechanism is correct and available to use.

CHAPTER III
METHODOLOGY

3.1 Software

1. Java Development Kit (Standard Edition) version 8u171
2. Eclipse (Integrated Development Environment)

3.2 Kinetic Model

The kinetic model of C_1 and C_2 formation in the Fischer-Tropsch synthesis reaction over the cobalt catalyst was established by applying the reaction mechanisms of Storsæter *et al*. (2006). According to the literature, two reaction models including the carbide mechanism and the CO insertion mechanism were based on the Langmuir-Hinshelwood approach. The models consisted of the associative adsorption of CO, the dissociative adsorption of H_2, the dissociation of adsorbed CO, the formation of CH_4, the first chain growth producing C_2H_6 and C_2H_4, and the Water-Gas Shift reaction. However, the productions of other hydrocarbon types and the adsorption of all products were ignored in this work.

The mechanism of C_1 and C_2 formation based on the carbide mechanism could be described by a 25-step elementary reaction (Table 3.1). The step 1 to step 19 described the Fischer-Tropsch synthesis reaction on the surface of cobalt metal. The Water-Gas Shift reaction occurs in step 20 to step 25. Moreover, the kinetic parameters of each elementary step were summarized in Table 3.1. According to these parameters, step 8, 10, 15 and 17 were assumed to be instantaneous (probability of an event was equal to 1) because of their significantly low activation energies and high pre-exponential factors.

Table 3.1 Elementary reactions and corresponding kinetic parameters based on the carbide mechanism

Step	Elementary reaction	$A_{ads,i}$ or A_i ($bar^{-1}\cdot s^{-1}$ or s^{-1})	Ea_i (kJ/mol)
1	$CO_{(g)} + * \rightarrow CO*$	4.20×10^4 ($A_{ads,i}$)	0.0
2	$H_{2(g)} + 2* \rightarrow 2H*$	2.20×10^6 ($A_{ads,i}$)	14.1
3	$CO* \rightarrow CO_{(g)} + *$	1.00×10^{13}	111.6
4	$2H* \rightarrow H_{2(g)} + 2*$	1.90×10^{13}	75.0
5	$CH_3CH_3** \rightarrow C_2H_{6(g)} + 2*$	1.00×10^{13}	43.8
6	$CH_2CH_2** \rightarrow C_2H_{4(g)} + 2*$	1.00×10^{13}	55.3
7	$H_2O* \rightarrow H_2O_{(g)} + *$	1.13×10^{12}	51.0
8[a,b]	$CO_2** \rightarrow CO_{2(g)} + 2*$	1.00×10^{13}	27.7
9	$CO* + H* \rightarrow C* + OH*$	1.70×10^{14}	87.0
10[a,b]	$C* + H* \rightarrow CH* + *$	2.69×10^{13}	18.0
11	$CH* + H* \rightarrow CH_2* + *$	2.60×10^{13}	59.6
12	$CH_2* + H* \rightarrow CH_3* + *$	2.60×10^{13}	34.0
13	$CH_3* + H* \rightarrow CH_{4(g)} + 2*$	1.65×10^{12}	30.8
14	$CH_3* + CH* \rightarrow CH_3CH* + *$	5.50×10^{11}	25.0
15[a]	$CH_3* + CH_2* \rightarrow CH_3CH_2* + *$	4.50×10^{12}	5.4
16	$CH_3* + CH_3* \rightarrow CH_3CH_3* + *$	5.50×10^{11}	20.8
17[a]	$CH_3CH* + H* \rightarrow CH_3CH_2* + *$	2.10×10^{14}	37.4
18	$CH_3CH_2* + H* \rightarrow CH_3CH_3**$	6.70×10^{11}	29.1
19	$CH_3CH_2* + 2* \rightarrow CH_2CH_2** + H*$	1.00×10^{13}	42.0
20	$OH* + H* \rightarrow H_2O* + *$	1.10×10^{13}	36.5
21	$H_2O* + * \rightarrow OH* + H*$	1.00×10^{13}	90.9
22	$OH* + * \rightarrow O* + H*$	1.00×10^{13}	57.1
23	$O* + H* \rightarrow OH* + *$	1.10×10^{14}	108.4
24	$CO* + O* \rightarrow CO_2**$	7.70×10^{12}	62.2
25	$CO_2** \rightarrow CO* + O*$	1.00×10^{13}	47.7

Note: * is a vacant site, X* is an adsorbed X species occupying on a site, and X** is adsorbed X species occupying on two-adjacent site.

[a] Assumed instantaneous reaction

[b] Referenced from Asiaee *et al.* (2017)

For the CO insertion mechanism, a set of 27 elementary reactions and corresponding kinetic parameters were summarized in Table 3.2. The Fischer-Tropsch synthesis reactions were described in step 1 to step 21, and the Water-Gas Shift reactions were described in step 22 to step 27. Due to their significantly low activation energies and high pre-exponential factors, step 8, 11 and 17 were also assumed to be instantaneous reaction.

Table 3.2 Elementary reactions and corresponding kinetic parameters based on the CO insertion mechanism

Step	Elementary reaction	$A_{ads,i}$ or A_i (bar^{-1}·s^{-1} or s^{-1})	Ea_i (kJ/mol)
1	$CO_{(g)} + * \rightarrow CO*$	4.20×10^4 ($A_{ads,i}$)	0.0
2	$H_{2(g)} + 2* \rightarrow 2H*$	2.20×10^6 ($A_{ads,i}$)	14.1
3	$CO* \rightarrow CO_{(g)} + *$	1.00×10^{13}	111.6
4	$2H* \rightarrow H_{2(g)} + 2*$	1.90×10^{13}	75.0
5	$CH_3CH_3** \rightarrow C_2H_{6(g)} + 2*$	1.00×10^{13}	43.8
6	$CH_2CH_2** \rightarrow C_2H_{4(g)} + 2*$	1.00×10^{13}	55.3
7	$H_2O* \rightarrow H_2O_{(g)} + *$	1.13×10^{12}	51.0
8[a,b]	$CO_2** \rightarrow CO_{2(g)} + 2*$	1.00×10^{13}	27.7
9	$CO* + H* \rightarrow HCO* + *$	1.70×10^{14}	87.0
10	$HCO* + H* \rightarrow H_2CO* + *$	2.70×10^{12}	51.9
11[a,b]	$H_2CO* + H* \rightarrow H_3CO* + *$	2.10×10^{13}	14.6
12	$H_3CO* + H* \rightarrow CH_3* + OH*$	2.60×10^{13}	82.7
13	$H_3CO* + * \rightarrow CH_3* + O*$	1.00×10^{13}	57.6
14	$CH_3* + H* \rightarrow CH_{4(g)} + 2*$	1.65×10^{12}	30.8

Step	Elementary reaction	$A_{ads,i}$ or A_i ($bar^{-1}\cdot s^{-1}$ or s^{-1})	Ea_i (kJ/mol)
15	$CH_3^* + CO^* \rightarrow CH_3CO^* + *$	7.30×10^{13}	54.0
16	$CH_3CO^* + H^* \rightarrow CH_3CHO^* + *$	4.70×10^{12}	52.2
17[a,b]	$CH_3CHO^* + H^* \rightarrow CH_3CH_2O^* + *$	4.60×10^{12}	30.3
18	$CH_3CH_2O^* + H^* \rightarrow CH_3CH_2^* + OH^*$	1.10×10^{13}	82.9
19	$CH_3CH_2O^* + * \rightarrow CH_3CH_2^* + O^*$	1.00×10^{13}	59.4
20	$CH_3CH_2^* + H^* \rightarrow CH_3CH_3^{**}$	6.70×10^{11}	29.1
21	$CH_3CH_2^* + 2^* \rightarrow CH_2CH_2^{**} + H^*$	1.00×10^{13}	42.0
22	$OH^* + H^* \rightarrow H_2O^* + *$	1.10×10^{13}	36.5
23	$H_2O^* + * \rightarrow OH^* + H^*$	1.00×10^{13}	90.9
24[b]	$OH^* + * \rightarrow O^* + H^*$	1.49×10^{14}	94.1
25[b]	$O^* + H^* \rightarrow OH^* + *$	1.72×10^{14}	63.6
26	$CO^* + O^* \rightarrow CO_2^{**}$	7.70×10^{12}	62.2
27	$CO_2^{**} \rightarrow CO^* + O^*$	1.00×10^{13}	47.7

Note: * is a vacant site, X* is an adsorbed X species occupying on a site, and X** is adsorbed X species occupying on a two-adjacent site.

[a] Assumed instantaneous reaction

[b] Referenced from Asiaee *et al.* (2017)

Moreover, the carbide and CO insertion mechanism were combined to suggest the possibility of each reaction mechanism. The elementary reactions and corresponding kinetic parameters were summarized in Table 3.3 and the instantaneous reactions (step 8, 10, 16, 20, 24 and 27) were the same reaction as two previous models.

Table 3.3 Elementary reactions and corresponding kinetic parameters based on combination between the carbide and CO insertion mechanism

Step	Elementary reaction	$A_{ads,i}$ or A_i ($bar^{-1}\cdot s^{-1}$ or s^{-1})	Ea_i (kJ/mol)
1	$CO_{(g)} + * \rightarrow CO^*$	4.20×10^4 ($A_{ads,i}$)	0.0

Step	Elementary reaction	$A_{ads,i}$ or A_i (bar^{-1}·s^{-1} or s^{-1})	Ea_i (kJ/mol)
2	$H_{2(g)} + 2* \rightarrow 2H*$	2.20×10^{6} ($A_{ads,i}$)	14.1
3	$CO* \rightarrow CO_{(g)} + *$	1.00×10^{13}	111.6
4	$2H* \rightarrow H_{2(g)} + 2*$	1.90×10^{13}	75.0
5	$CH_3CH_3** \rightarrow C_2H_{6(g)} + 2*$	1.00×10^{13}	43.8
6	$CH_2CH_2** \rightarrow C_2H_{4(g)} + 2*$	1.00×10^{13}	55.3
7	$H_2O* \rightarrow H_2O_{(g)} + *$	1.13×10^{12}	51.0
8[a,b]	$CO_2** \rightarrow CO_{2(g)} + 2*$	1.00×10^{13}	27.7
9	$CO* + H* \rightarrow C* + OH*$	1.70×10^{14}	87.0
10[a,b]	$C* + H* \rightarrow CH* + *$	2.69×10^{13}	18.0
11	$CH* + H* \rightarrow CH_2* + *$	2.60×10^{13}	59.6
12	$CH_2* + H* \rightarrow CH_3* + *$	2.60×10^{13}	34.0
13	$CH_3* + H* \rightarrow CH_{4(g)} + 2*$	1.65×10^{12}	30.8
14	$CO* + H* \rightarrow HCO* + *$	1.70×10^{14}	89.9
15	$HCO* + H* \rightarrow H_2CO* + *$	2.70×10^{12}	51.9
16[a,b]	$H_2CO* + H* \rightarrow H_3CO* + *$	2.10×10^{13}	14.6
17	$H_3CO* + H* \rightarrow CH_3* + OH*$	2.60×10^{13}	82.7
18	$H_3CO* + * \rightarrow CH_3* + O*$	1.00×10^{13}	57.6
19	$CH_3* + CH* \rightarrow CH_3CH* + *$	5.50×10^{11}	25.0
20[a]	$CH_3* + CH_2* \rightarrow CH_3CH_2* + *$	4.50×10^{12}	5.4
21	$CH_3* + CH_3* \rightarrow CH_3CH_3* + *$	5.50×10^{11}	20.8
22	$CH_3* + CO* \rightarrow CH_3CO* + *$	7.30×10^{13}	54.0
23	$CH_3CO* + H* \rightarrow CH_3CHO* + *$	4.70×10^{12}	52.2
24[a,b]	$CH_3CHO* + H* \rightarrow CH_3CH_2O* + *$	4.60×10^{12}	30.3
25	$CH_3CH_2O* + H* \rightarrow CH_3CH_2* + OH*$	1.10×10^{13}	82.9
26	$CH_3CH_2O* + * \rightarrow CH_3CH_2* + O*$	1.00×10^{13}	59.4
27[a]	$CH_3CH* + H* \rightarrow CH_3CH_2* + *$	2.10×10^{14}	37.4
28	$CH_3CH_2* + H* \rightarrow CH_3CH_3**$	6.70×10^{11}	29.1
29	$CH_3CH_2* + 2* \rightarrow CH_2CH_2** + H*$	1.00×10^{13}	42.0
30	$OH* + H* \rightarrow H_2O* + *$	1.10×10^{13}	36.5

Step	Elementary reaction	$A_{ads,i}$ or A_i ($bar^{-1}\cdot s^{-1}$ or s^{-1})	Ea_i (kJ/mol)
31	$H_2O^* + * \rightarrow OH^* + H^*$	1.00×10^{13}	90.9
32	$OH^* + * \rightarrow O^* + H^*$	1.00×10^{13}	57.1
33	$O^* + H^* \rightarrow OH^* + *$	1.72×10^{14}	63.6
34	$CO^* + O^* \rightarrow CO_2^{**}$	7.70×10^{12}	62.2
35	$CO_2^{**} \rightarrow CO^* + O^*$	1.00×10^{13}	47.7

Note: * is a vacant site, X* is an adsorbed X species occupying on a site, and X** is adsorbed X species occupying on two-adjacent site.

[a] Assumed instantaneous reaction

[b] Referenced from Asiaee *et al.* (2017)

The rate constants for adsorption (k_i) of molecule CO and H_2 in step 1 and 2 (Table 3.1, 3.2 and 3.3) could be calculated by equation (3.1), where $A_{ads,i}$ is the pre-exponential factor for adsorption of reactant in step i, P_i is the partial pressure of reactant in gas feed, R is the universal gas constant, T is the reaction temperature, and Ea_i is the energy barrier (Hansen *et al*., 2000).

$$k_i = A_{ads,i} P_i \exp\left(\frac{-Ea_i}{RT}\right) \tag{3.1}$$

The reaction rate constants for step i (k_i) excluding the instantaneous reactions could be calculated by the Arrhenius equation as shown in equation (3.2), where A_i is the pre-exponential factor.

$$k_i = A_i \exp\left(\frac{-Ea_i}{RT}\right) \tag{3.2}$$

3.3 Simulation Procedure

In the simulation, the kinetic models were performed on the surface of hexagonal close-packed cobalt metal. It was represented by a two-dimensional rhombic lattice of $L \times L$ sites (Figure 3.1) with the periodic boundary conditions to avoid the effect of catalyst edge. The surface presented only one type of active site, and contacted with an infinite reservoir of CO and H_2 gas molecules with a fixed proportion

of CO and H_2. The surface reactions took place only between six nearest neighboring sites.

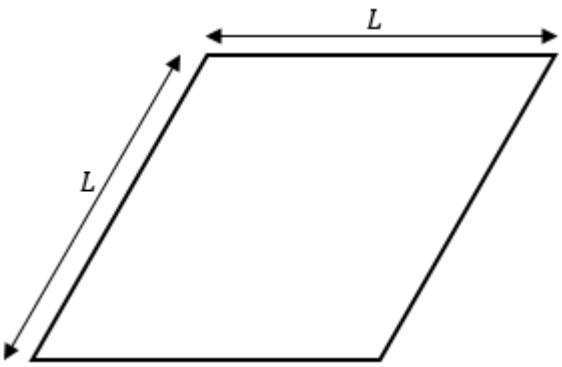

Figure 3.1 Drawing of two-dimensional rhombic lattice of $L \times L$ sites

The KMC algorithm to simulate the Fischer-Tropsch synthesis mechanisms on the cobalt surface was similar to that of Pruksawan *et al*. (2016). All simulations were started from empty surface lattice and computational time (t) of zero. The algorithm was demonstrated in Figure 3.2 and performed by the following steps:

(a) Randomly choose an active site from the surface.

(b) Perform each of instantaneous reaction events (step 8, 10, 15 and 17 in Table 3.1; step 8, 11 and 17 in Table 3.2; step 8, 10, 16, 20, 24 and 27 in Table 3.3) if possible. Namely, if the site selected from step (a) is occupied by a particle of reactants corresponding to any instantaneous reactions, and one of the neighboring sites is occupied by another species of reactants corresponding to the same reaction, that reaction event can be performed immediately. Two reactant particles are then replaced by the products according to the reaction. However, to check six nearest neighbor sites whether there is a possible event or not, each neighbor site is randomly checked until meeting the desired reactant species, or until all six sites.

(c) Choose a reaction event j from the elementary step i (i = 1 to 7, 9, 11 to 14, 16 and 18 to 25 for Table 3.1; i = 1 to 7, 9, 10, 12 to 16 and 18 to 27 for Table 3.2; i = 1 to 7, 9, 11 to 15, 17 to 19, 21 to 23, 25, 26, 28 to 35 for Table 3.3) according to $\sum_{i=1}^{j-1} p_i \leq r_1 < \sum_{i=1}^{j} p_i$, where r_1 is a uniformly distributed random number with a

value between 0 and 1, p_i is the probability of an event i determined by individual rate constant (k_i) per summation of all rate constant ($\sum k_i$) following Equation (3.3).

$$p_i = \frac{k_i}{\sum k_i} \tag{3.3}$$

(d) Perform the reaction event *j* selected from step (c) according to individual process types following:

(I) Adsorption event

- If the event *j* is the associative adsorption of CO (step 1) and the site selected from step (a) is vacant, the event can then be performed. The CO adsorption takes place and a particle of CO* is placed on the site. If the site is not vacant, skip to step (e).

- If the event *j* is the dissociative adsorption of H_2 (step 2) and the site selected from (a) is vacant, each neighboring site is randomly checked until meeting a vacant site. The event can then be performed, and the H_2 adsorption takes place. A particle of H* is placed on each of two adjacent vacant sites. If the site or all neighbor is not vacant, skip to step (e).

(II) Desorption event

- If the event *j* is the desorption of CO or H_2O (respective step 3 and 7) and the site selected from step (a) is occupied by a particle of CO* or H_2O*, the event can then be performed. The CO or H_2O desorption takes place, the site becomes vacant and a molecule of CO or H_2O leaves the surface. If the site is not occupied by a CO* or H_2O* particle, skip to step (e).

- If the event *j* is the desorption of C_2H_6 or C_2H_4 (respective step 5 and 6) and the site selected from step (a) is occupied by a carbon atom of CH_3CH_3** or CH_2CH_2** particle, each neighboring site is randomly checked until meeting another half of CH_3CH_3** or CH_2CH_2** particle. The event can then be performed, and the C_2H_6 or C_2H_4 adsorption takes place. Two adjacent sites occupied by a CH_3CH_3** or CH_2CH_2** become vacant and a molecule of C_2H_6 or C_2H_4 leaves the surface. If the site is not occupied with a part of CH_3CH_3** particle, skip to step (e).

- If the event j is the associative desorption of H_2 and the site selected from step (a) is occupied by a particle of H*, each neighboring site is randomly checked until meeting another H* particle. The event can then be performed, and the H_2 desorption takes place. Two adjacent sites occupied by H* become vacant and a molecule of H_2 leaves the surface. If either site is not occupied with a H* particle, skip to step (e).

(III) Surface reaction event

- If the event j is the surface reaction (step 9, 11, 12, 14, 16 or 18 to 25 in Table 3.1; step 9, 10, 12, 13, 15, 16 or 18 to 27 in Table 3.2; step 9, 11, 12, 14, 15, 17 to 19, 21 to 23, 25, 26, 28 to 35 in Table 3.3) and the site selected from step (a) is occupied by a particle of reactants corresponding to reaction selected from step (c), each neighboring site is checked randomly until meeting a site occupied by another species of reactants corresponding to the same reaction. The event j can then be performed, and the surface reaction takes place. Two adjacent sites occupied by reactants is replaced by the product particles corresponding to the reaction. If either site is not occupied by the appropriate reactant, skip to step (e).

- If the event j is the formation of CH_4 along with CH_4 desorption (step 13 in Table 3.1 and 3.3; step 14 in Table 3.2) and the site selected from step (a) is occupied by a particle of either CH_3* or H*, each neighboring site is checked randomly until meeting a site occupied by CH_3* or H* (differing from the previous site). The event j can then be performed, and the CH_4 formation takes place. Two adjacent sites occupied by CH_3* and H* become vacant and a molecule of CH_4 leaves the surface immediately. If either site is not occupied by CH_3* or H* particles, skip to step (e).

(e) Update time t to be $t+\Delta t$. The time interval (Δt) can be estimated by equation (3.4), where r_2 is a uniformly distributed random number with a value between 0 and 1, L^2 is the total number of active sites.

$$\Delta t = \frac{-\ln r_2}{L^2 \cdot \sum k_i} \tag{3.4}$$

(f) Repeat the algorithm since step (a), which is one Monte-Carlo cycle, until the steady state is reached.

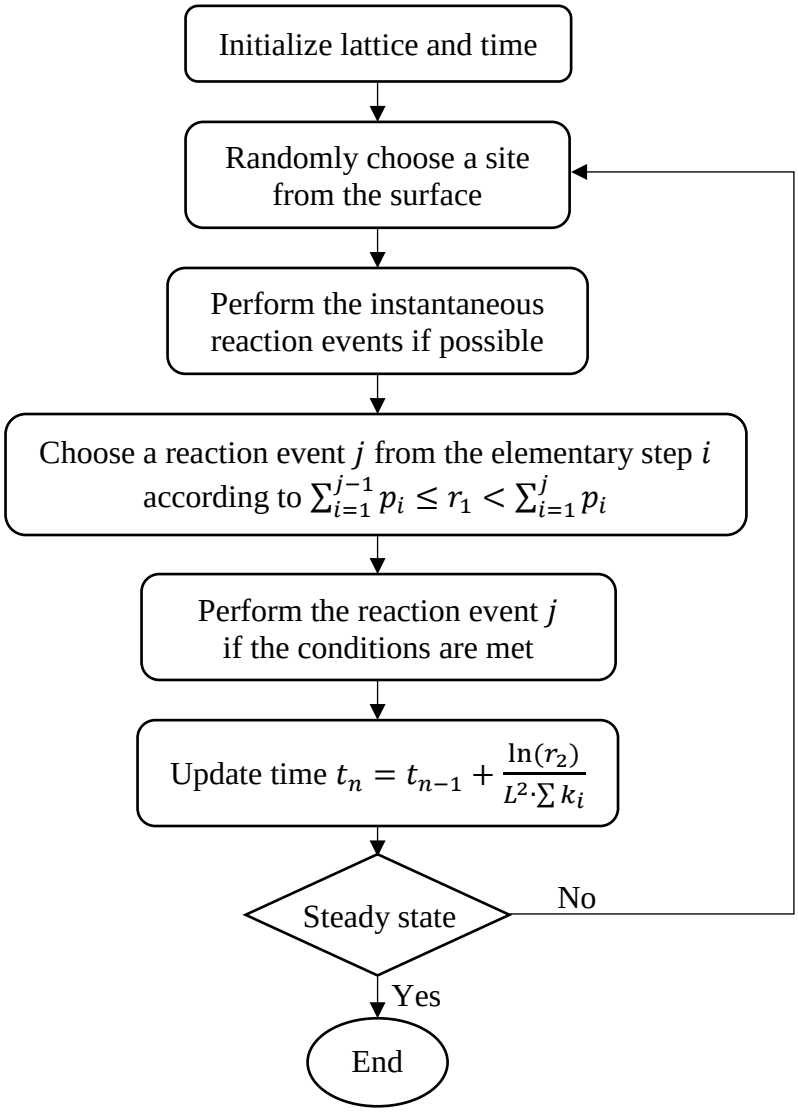

Figure 3.2 KMC algorithm used in this work

In the simulation, the production rate (R_i), selectivity (S_i) and fractional coverage (θ_i) were calculated in every cycle. The fractional coverages of each adsorbed species could be determined by the number of individual adsorbed particles over the lattice site per the total number of active sites. The production rates of CH_4, C_2H_6, C_2H_4, H_2O and CO_2 were defined by the number of individual produced molecule per lattice site per unit time. The selectivity of hydrocarbon product i (i = CH_4, C_2H_6 or C_2H_4) could be computed by equation (3.5).

$$S_i = \frac{R_i}{R_{CH_4} + R_{C_2H_6} + R_{C_2H_4}} \tag{3.5}$$

In order to avoid non-equilibrium behavior, several million Monte-Carlo cycles were necessary to be run. The production rate, selectivity and fractional coverage were reported by taking the averages of these values of about 300,000 cycles after the steady state point.

All mechanisms (Table 3.1, 3.2 and 3.3) were initially simulated with the cobalt surface (without inactive impurity on the surface) containing 128×128 sites, and the reaction conditions were defined at 493 K, 15 bar, and H_2/CO feed molar ratio of 2.1, according to the experimental conditions of Todic *et al*. (2014). The appropriate mechanism either carbide or CO insertion was then suggested and used to study the influences of reaction conditions. The temperature (T), pressure (P) and H_2/CO feed molar ratio (H_2/CO) were adjusted in the ranges as shown in Table 3.4.

Table 3.4 Ranges of simulation parameters

Parameter	Value
Temperature (T)	453 – 508 K
Pressure (P)	11 – 35 bar
H_2/CO feed molar ratio (H_2/CO)	0.6 – 6.1

CHAPTER IV
RESULTS AND DISCUSSION

To study the Fischer-Tropsch synthesis taking place over the surface of the catalyst, Kinetic Monte-Carlo (KMC) simulation is used by applying two reaction mechanisms, which are the carbide mechanism (Table 3.1) and the CO insertion mechanism (Table 3.2). Those two mechanisms are combined (Table 3.3) to investigate the possibility of each reaction mechanism, and the appropriate mechanism in this study is then suggested. In addition, the effects of reaction temperature (T), pressure (P), H_2/CO feed molar ratio (H_2/CO) were also investigated.

4.1 Transient Simulations

Due to the different equilibrium point in each mechanism, the models are simulated for several million Monte-Carlo cycles until the results reach the state steady. It is important to check this point in each simulation to avoid non-equilibrium behavior.

For the simulation based on the carbide mechanism, the calculations of the production rates and the fractional coverages of the adsorbed species are carried out in every Monte-Carlo cycle. Figure 4.1 illustrates the production rates of CH_4, C_2H_6, C_2H_4, H_2O and CO_2 changing over the computational time. It can be observed that the rates suddenly increase at the beginning and then reach steady state within about 0.06 milliseconds (dashed line). After this point, the surface is in equilibrium leading to constant surface coverages, and all products are formed with stable production rate. The relationship between fractional coverages and time is showed in Figure 4.2. According to the results, the adsorbed reactants (H* and CO*) are mainly found on the surface of metallic cobalt with the small presence of the other species. However, some fluctuations in the coverage curves are observed, which may be caused by the statistical noises during the simulation.

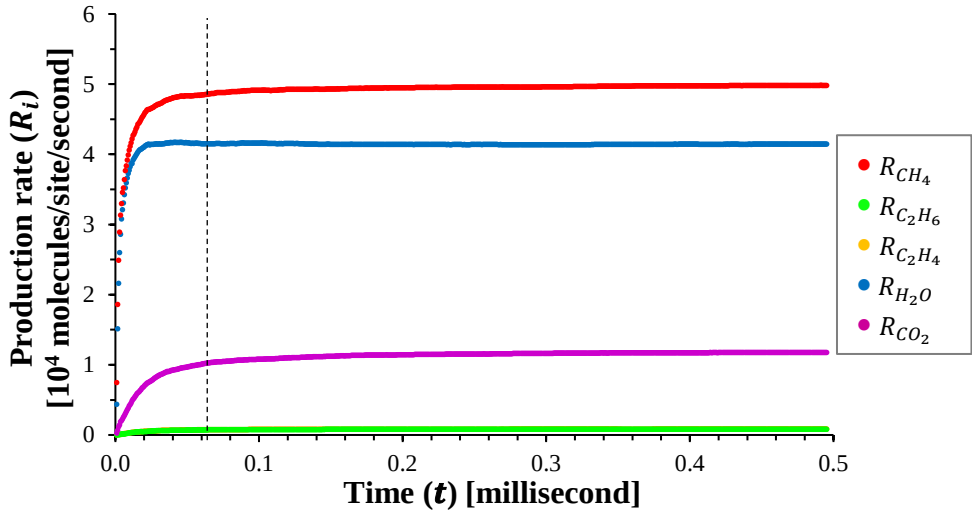

Figure 4.1 Production rates as a function of time from carbide mechanism; T = 493 K, P = 15 bar and H_2/CO = 2.1

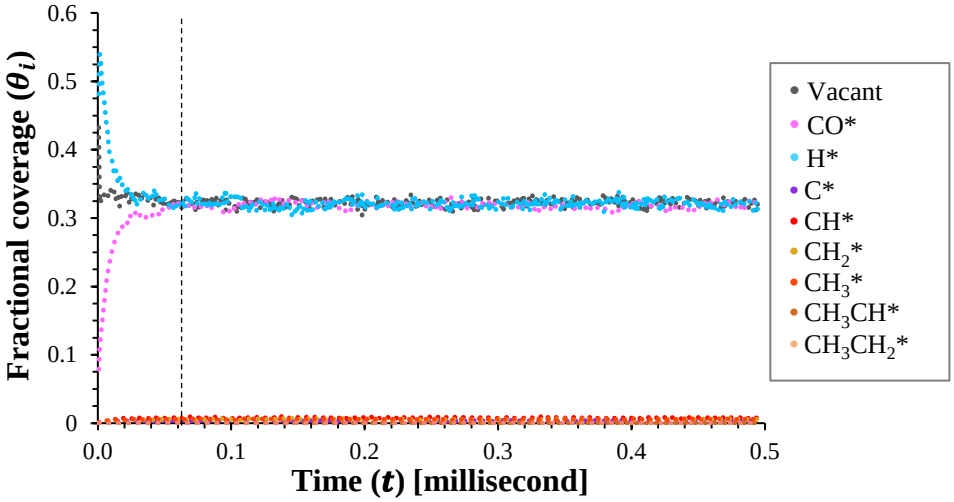

Figure 4.2 Fractional coverages of adsorbed reactants and hydrocarbon intermediates as a function of time from carbide mechanism; T = 493 K, P = 15 bar and H_2/CO = 2.1

From the results of the CO insertion mechanism, the production rates and the fractional coverages as a function of time are revealed in Figure 4.3 and 4.4, respectively. The results present that the system reaches the equilibrium within around 0.06

milliseconds (Figure 4.3). The surface is covered with CO* and H* particles predominantly (Figure 4.4) as also seen in the carbide mechanism.

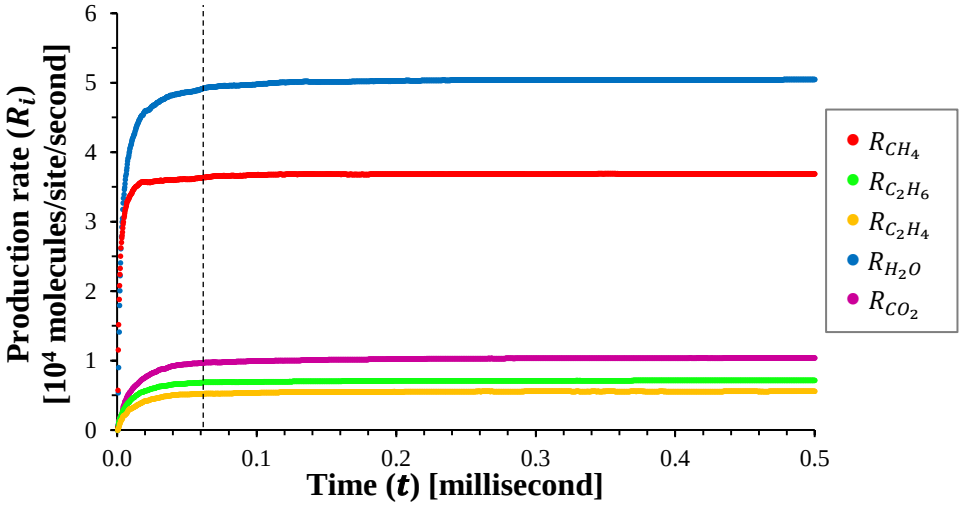

Figure 4.3 Production rates as a function of time from CO insertion mechanism; T = 493 K, P = 15 bar and H_2/CO = 2.1

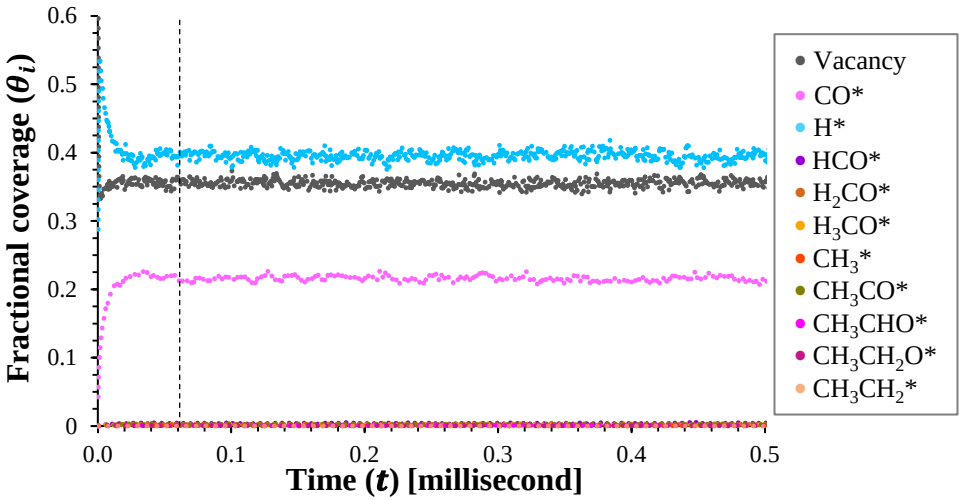

Figure 4.4 Fractional coverages of adsorbed reactants and hydrocarbon intermediates as a function of time from CO insertion mechanism; T = 493 K, P = 15 bar and H_2/CO = 2.1

For the simulation based on the combination between the carbide and CO insertion mechanism, the production rates and the fractional coverages as a function of time are exhibited in Figure 4.5 and 4.6. The system in this model reaches the steady state within 0.06 milliseconds (Figure 4.5). According to the results, CO*, H* and vacant site are found in a high proportion on the surface with very small number of intermediate species as demonstrated in Figure 4.6.

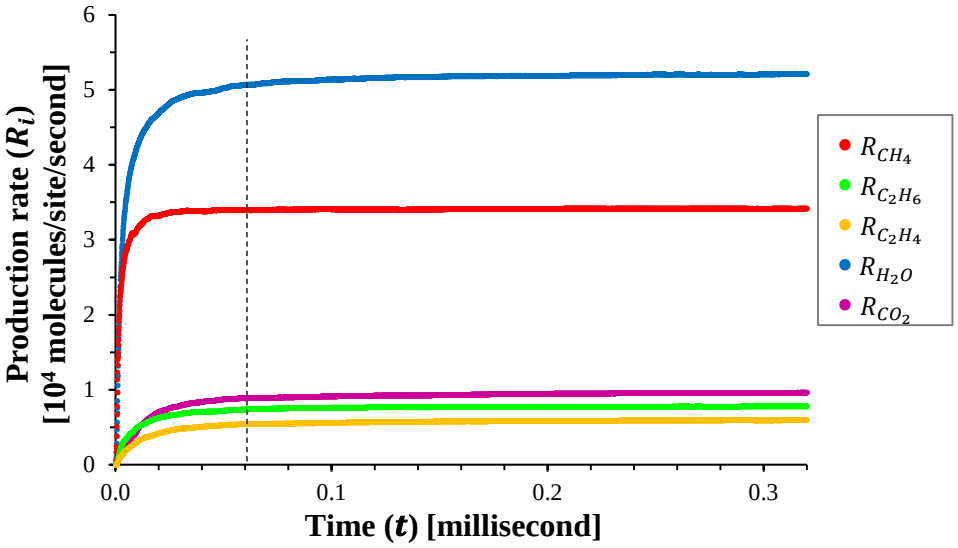

Figure 4.5 Production rates as a function of time from combination between carbide and CO insertion mechanism; T = 493 K, P = 15 bar and H_2/CO = 2.1

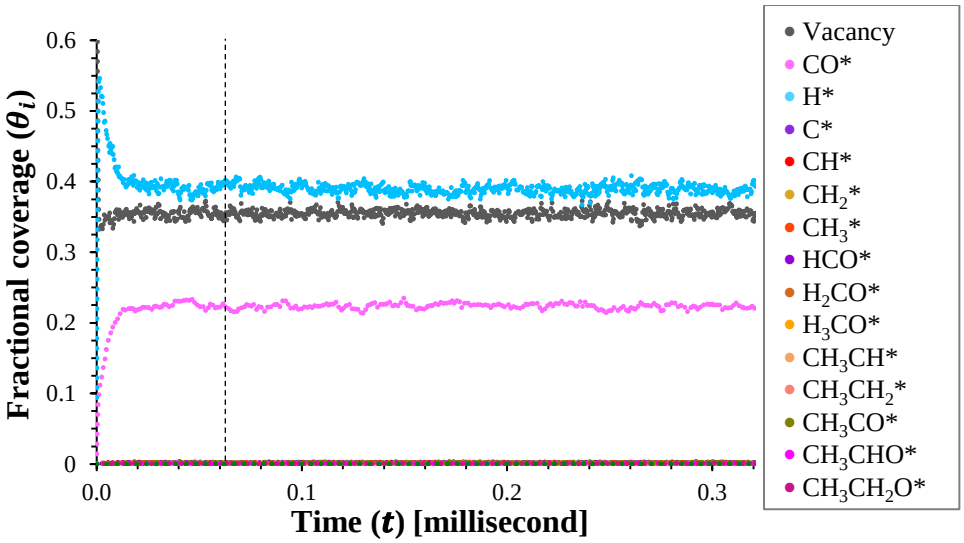

Figure 4.6 Fractional coverages of adsorbed reactants and hydrocarbon intermediates as a function of time from combination between carbide and CO insertion mechanism; T = 493 K, P = 15 bar and H_2/CO = 2.1

4.2 Investigation of Fischer-Tropsch Synthesis Mechanism

To study the kinetics of the Fischer-Tropsch synthesis, the detailed mechanism in the reaction is required to be clear. Three reaction models (Table 3.1, 3.2 and 3.3) are simulated and compared the results to one another.

From simulation results, Figure 4.7 shows the snapshots of the cobalt surface obtained from different simulations under the steady state. In all investigated reaction models, it can be observed that the surface is predominantly covered with H* (blue) and CO* (pink), while other species present in much small number on the surface. Moreover, the fraction of H* and CO* on the surface from the CO insertion mechanism (Figure 4.7b) is similar to the combination between the carbide and CO insertion mechanism (Figure 4.7c). The surface from the carbide mechanism (Figure 4.7a) exhibits a high proportion of CO*.

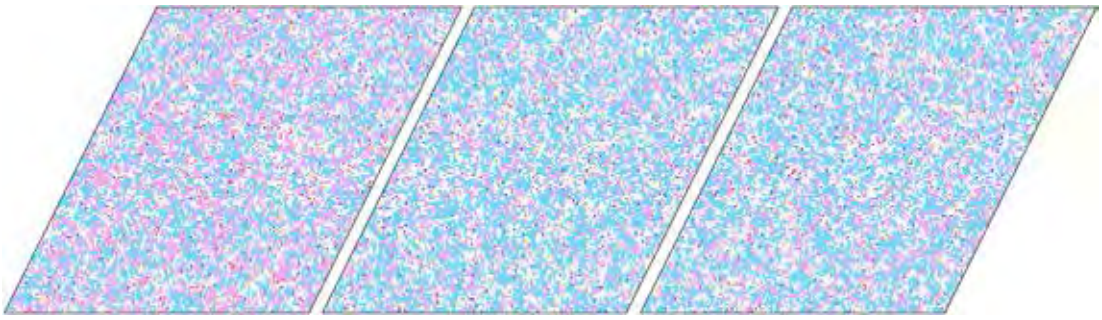

(a) (b) (c)

Figure 4.7 Snapshots of the surface from (a) carbide mechanism, (b) CO insertion mechanism and (c) combined carbide and CO insertion mechanism; T = 493 K, P = 15 bar and H_2/CO = 2.1 (□ = Vacant site, ■ = CO*, ■ = H*, ■ = C*, ■ = CH*, ■ = CH_2*, ■ = CH_3*, ■ = HCO*, ■ = H_2CO*, ■ = H_3CO*, ■ = CH_3CH*, ■ = CH_3CH_2*, ■ = CH_3CO*, ■ = CH_3CHO*, ■ = CH_3CH_2O*, ■ = O*, ■ = OH*, ■ = H_2O*)

The production rates, C_1/C_2 product ratio and fractional coverages of reactants from each simulation under the steady state are presented in Table 4.1. According to the carbide mechanism, C_2 products are produced in low production rate of 0.17×10^4 molecules/site/second when compared to that of the other models. The production rate of CH_4 presents quite high (5.00×10^4 molecules/site/second). The reason is that the CH_x* intermediates (x = 0-3), which are the monomer species reacting each other to form C-C bond (step 14 to step 16 in Table 3.1), present on the cobalt surface in a very small amount. Since the C-C bonding is difficult to occur through the carbide mechanism, the CH_4 formation (step 10 to step 13 in Table 3.1) is a favorable route on the surface.

For the CO insertion mechanism, the CO* is directly used for forming C-C bond in the chain growth step (step 15 in Table 3.2). Since the CO* is found in high proportion on the surface, the formation of the C-C bond in the CO insertion mechanism is easier than that of the carbide mechanism. In addition, it can also be observed that the results from the CO insertion mechanism are nearly equivalent to the combined mechanism. Accordingly, although the carbide mechanism and the CO insertion mech-

anism are performed together in a simulation, the reaction pathway is performed similarly to the CO insertion mechanism. This can be proved by investigating the possibility of each reaction mechanism in the combined mechanism model.

Table 4.1 Production rates, C_1/C_2 product ratio and fractional coverages with different mechanism; T = 493 K, P = 15 bar and H_2/CO = 2.1 (steady state)

Kinetic parameter	Reaction mechanism		
	Carbide	**CO insertion**	**Combination**
Production rate (R_i)			
[10^4 molecules/site/second]			
R_{CH_4}	5.00	3.69	3.42
$R_{C_2H_6}$	0.08	0.72	0.78
$R_{C_2H_4}$	0.09	0.56	0.60
R_{H_2O}	4.16	5.06	5.21
R_{CO_2}	1.19	1.04	0.96
Product ratio			
C_1/C_2	28.81	2.88	2.48
Fractional coverage (θ_i)			
θ_{Vacant}	0.3218	0.3542	0.3571
θ_{CO}	0.3199	0.2138	0.2230
θ_H	0.3198	0.3962	0.3871

The simulation based on the combined carbide and CO insertion mechanism is adjusted the reaction conditions according to the Fischer-Tropsch conditions in the literature of Todic *et al.*, (2014). The comparison results of the C_1/C_2 product ratio between simulation and experiment under the same conditions are summarized in Table 4.1. It can be seen that the C_1/C_2 product ratios obtained from the simulation are lower than those of the experiment. The important reason is the neglected re-adsorption of all products for the simulation in this work, but the particular C_2H_4 can actually be re-adsorbed on the catalyst surface and formed the longer carbon chain in the

Fischer-Tropsch synthesis reaction. The re-adsorption of C_2H_4 significantly leads to a decrease in the proportion of C_2 products, as reported in several researches (Förtsch *et al*., 2015; Pour *et al*., 2013; Todic *et al*., 2013).

Table 4.2 Possibility of carbide and CO insertion mechanism in the simulation based on combined carbide and CO insertion mechanism and C_1/C_2 product ratio from results of simulation and experiment in literature of Todic et al., 2014

Reaction condition			**C_1/C_2 product**		**Possibility (%)**	
T [K]	P [bar]	H_2/CO	**Experiment**	**This study**	**Carbide**	**CO insertion**
493	15	1.4	6.96	1.24	4.00	96.00
493	15	2.1	8.06	2.48	3.10	96.90
493	25	2.1	5.91	2.24	3.08	96.92
503	15	1.4	6.47	1.47	4.07	95.93
503	15	2.1	7.57	2.94	3.65	96.35
503	25	1.4	5.40	1.33	3.84	96.16
503	25	2.1	6.81	3.94	2.79	97.21

In all cases of the simulation based on the combined mechanism, the formation rates of C_2 intermediates on the surface, which are CH_3CH^*, $CH_3CH_2^*$, $CH_3CH_3^*$ (respective step 19, 20, 21 and 22 in Table 3.3), were computed. The rates of CH_3CH^*, $CH_3CH_2^*$ and $CH_3CH_3^*$ indicate the possibility of the carbide mechanism path, while the CH_3CO^* formation represents the CO insertion mechanism path. Table 4.2 also reveals the possibility of each mechanism path occurring in the combined mechanism. It is clearly observed that the C_2 intermediates are mainly produced through the CO insertion mechanism in all conditions, even though the rate constants for the formation of CH_3CH^*, $CH_3CH_2^*$ and $CH_3CH_3^*$ are higher than that of CH_3CO^*. This is because of the difference of fractional coverage of individual monomer species required in each reaction mechanism. It can also be said that the kinetics of the Fischer-Tropsch synthesis reaction is not only controlled by the kinetic rate constant, but also by the surface coverage (Tian *et al*., 2010).

According to the simulation results, the formation of C−C bond for the production of C_2 products is mainly carried out by the insertion of adsorbed CO into a metal–methyl bond. It is used to establish the simulation to study the kinetic behavior of the Fischer-Tropsch synthesis in present work.

4.3 Effect of Lattice Size

In the simulation, the edge effect is avoided by defining the periodic boundary conditions. It can be checked by adjusting the lattice size, from 128×128 to 32×32, 64×64 and 256×256. The production rates, selectivities of hydrocarbon products, and fractional coverages of adsorbed reactants and hydrocarbon intermediates obtained from each lattice size are shown in Table 4.3.

Table 4.3 Production rates, selectivities and fractional coverages with various sizes of lattice; T = 493 K, P = 15 bar and H_2/CO = 2.1 (steady state)

Kinetic parameter	**Lattice size**			
	32×32	**64×64**	**128×128**	**256×256**
Production rate (R_i)				
[10^4 molecules/site/second]				
R_{CH_4}	3.68	3.68	3.69	3.69
$R_{C_2H_6}$	0.72	0.73	0.72	0.71
$R_{C_2H_4}$	0.57	0.56	0.56	0.56
R_{H_2O}	5.06	5.07	5.06	5.05
R_{CO_2}	1.05	1.04	1.04	1.02
Selectivity (S_i)				
S_{CH_4}	0.74	0.74	0.74	0.74
$S_{C_2H_6}$	0.14	0.15	0.14	0.14
$S_{C_2H_4}$	0.11	0.11	0.11	0.11
Fractional coverage (θ_i)				
θ_{Vacant}	0.3510	0.3534	0.3542	0.3549

Kinetic parameter	Lattice size			
	32×32	**64×64**	**128×128**	**256×256**
θ_{CO}	0.2162	0.2115	0.2138	0.2144
θ_{H}	0.3945	0.3984	0.3962	0.3959
θ_{HCO}	0.0040	0.0038	0.0039	0.0039
θ_{H_2CO}	0.0027	0.0023	0.0025	0.0024
θ_{H_3CO}	0.0016	0.0017	0.0017	0.0017
θ_{CH_3}	0.0004	0.0005	0.0005	0.0005
θ_{CH_3CO}	0.0025	0.0023	0.0025	0.0025
θ_{CH_3CHO}	0.0011	0.0011	0.0011	0.0011
$\theta_{CH_3CH_2O}$	0.0007	0.0006	0.0007	0.0007
$\theta_{CH_3CH_2}$	0.0001	0.0001	0.0001	0.0001

From the simulation results, it is clearly seen that the values of the production rates, selectivities and fractional coverages at different lattice sizes are insignificantly different. However, lattice sizes of 32×32 and 64×64 sites are too small system. It means that the results exhibit large fluctuations, because the KMC simulation is a stochastic method. A large lattice size of 256×256 sites is also not necessary in order to save the computational time. Therefore, a lattice size of 128×128 sites is selected in this work to investigate the effects of reaction conditions.

4.4 Effect of Reaction Temperature

The production rates of produced CH_4, C_2H_6, C_2H_4, H_2O and CO_2 are evaluated with the various temperatures between 453 and 508 K at the desired pressure of 15 bar and H_2/CO molar feed ratio of 2.1, as shown in Figure 4.8. It can be seen that the reaction occurs when the temperature is higher than 463 K. Below 463 K, the accumulation of various species on the catalyst surface is observed especially the reactants because of no reaction taking place. Figure 4.9 illustrates the relation between fractional coverages of reactants and temperature. It shows that CO* mostly occupies on the surface at low temperatures. In contrast, H* is not found on the surface. The

reason is that H* can be easily desorbed from the surface than CO* due to the lower desorption rate constant than that of CO (Asiaee *et al*., 2017). It causes a high accumulation of CO* on the surface, which is the reason for the non-reactive state.

As shown in Figure 4.8, the reactive states occur at temperature above 463 K. For these regions, the production rates of all products continuously increase with increasing temperature, as observed in the experimental result of Todic *et al*. (2014). The increasing temperature can promote the dissociation of CO* (step 9 to step 13 in Table 3.2) leading to the continuous decrease of CO* on the surface, as also reported by Visconti *et al*. (2011). Since the accumulation of CO* on the surface is reduced and the surface reactions continuously take place, the surface vacant sites are more left. The H_2 can then adsorb more on the surface leading to an increasing of fractional coverage of H*.

Not only the main products (CH_4, C_2H_6 and C_2H_4) but the formation rate of CO_2 is also slightly increased with increasing temperature (Figure 4.8). It can be said that the higher temperature is suitable for the Water-Gas Shift reaction (step 22 to step 27 in Table 3.2) to produce undesired CO_2.

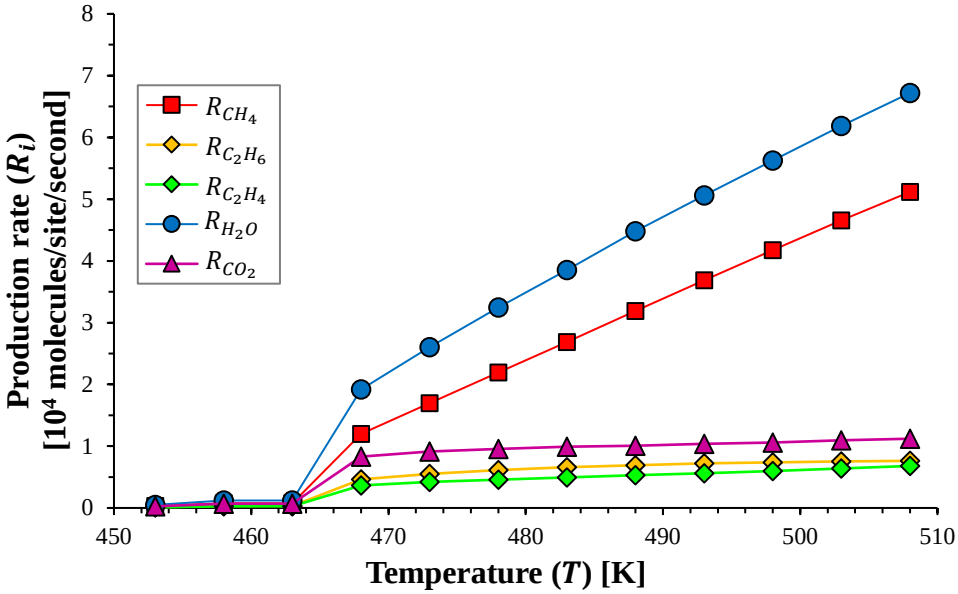

Figure 4.8 Production rates as a function of temperature; L = 128, P = 15 bar and H_2/CO = 2.1 (Steady state)

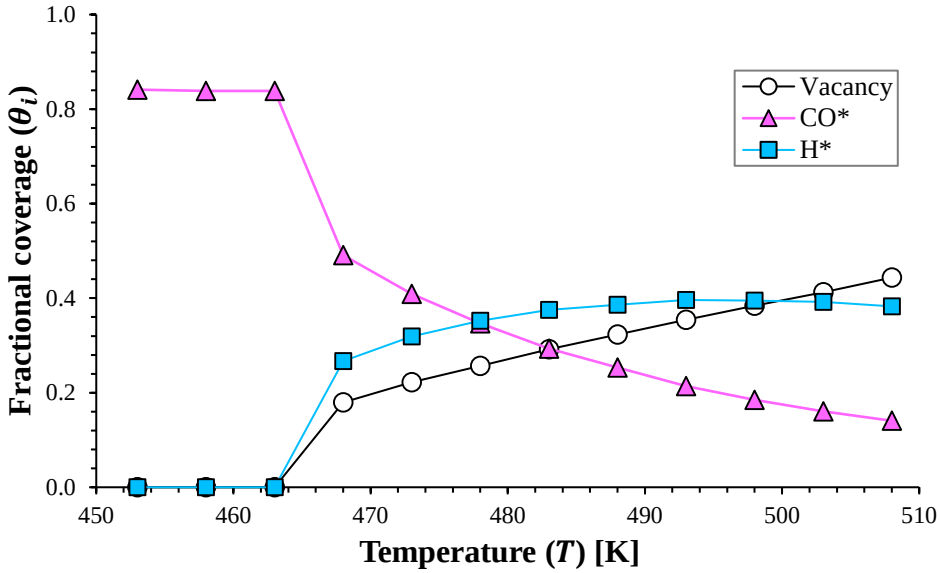

Figure 4.9 Vacant site and fractional coverages of CO* and H* as a function of temperature; $L = 128$, $P = 15$ bar and $H_2/CO = 2.1$ (Steady state)

Figure 4.10 shows the snapshots of the cobalt surface obtained from the simulation. The surface is saturated by CO* at temperature of 463 K as demonstrated in Figure 4.10a and the system becomes non-reactive. Figure 4.10b and 4.10c present the steady state of the systems at temperatures of 493 and 508 K, respectively. The number of vacant sites of Figure 4.10b is more than that of Figure 4.10c resulting from the decrease of CO* fractional coverage.

For the reactive regions at temperature higher than 463 K, while the formation rates of CH_4, C_2H_6 and C_2H_4 increase with increasing reaction temperature (Figure 4.8), the coverages of C_1 intermediate species (HCO*, H_2CO*, H_3CO* and CH_3*) and C_2 intermediate species (CH_3CO*, CH_3CHO*, CH_3CH_2O* and CH_3CH_2*) are significantly decreased, as can be seen in Figure 4.11. The coverages of those species exhibit negative trends with temperatures. It can be indicated that the hydrocarbon intermediates have a very short residence time on the cobalt surface at high temperature. This is because the increment of H* on the surface (Figure 4.9) can provide more chance for hydrogenation of hydrocarbons on the surface resulting in more CH_4, C_2H_6 and C_2H_4 products leaving from the surface.

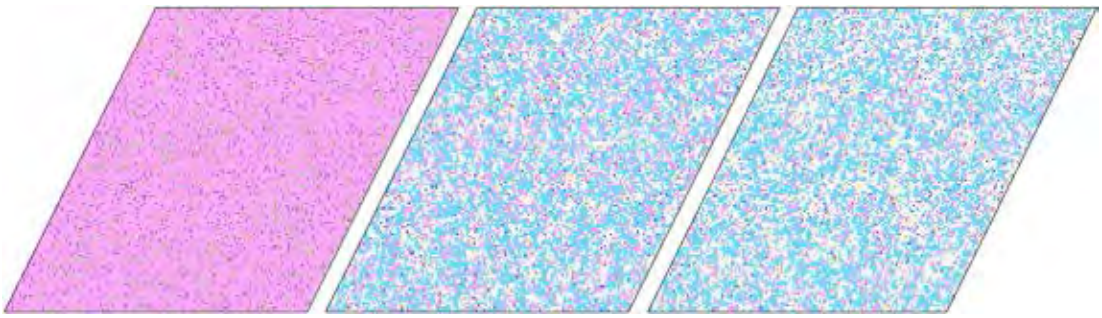

(a) (b) (c)

Figure 4.10 Snapshots of the surface at (a) T = 463 K, (b) T = 493 K and (c) T = 508 K; L = 128, P = 15 bar and H_2/CO = 2.1 (□ = Vacant site, ■ = CO*, ■ = H*, ■ = HCO*, ■ = H_2CO*, ■ = H_3CO*, ■ = CH_3*, ■ = CH_3CO*, ■ = CH_3CHO*, ■ = CH_3CH_2O*, ■ = CH_3CH_2*, ■ = O*, ■ = OH*, ■ = H_2O*)

Furthermore, the fractional coverages of CO* in Figure 4.9 has a similar trend to those of C_2 intermediate species. The decrease in CO* on the surface can reduce the formation of C_2 intermediates. The simulation results indicate that CO* is the important species for the hydrocarbon chain growth corresponding to the theory of CO insertion mechanism.

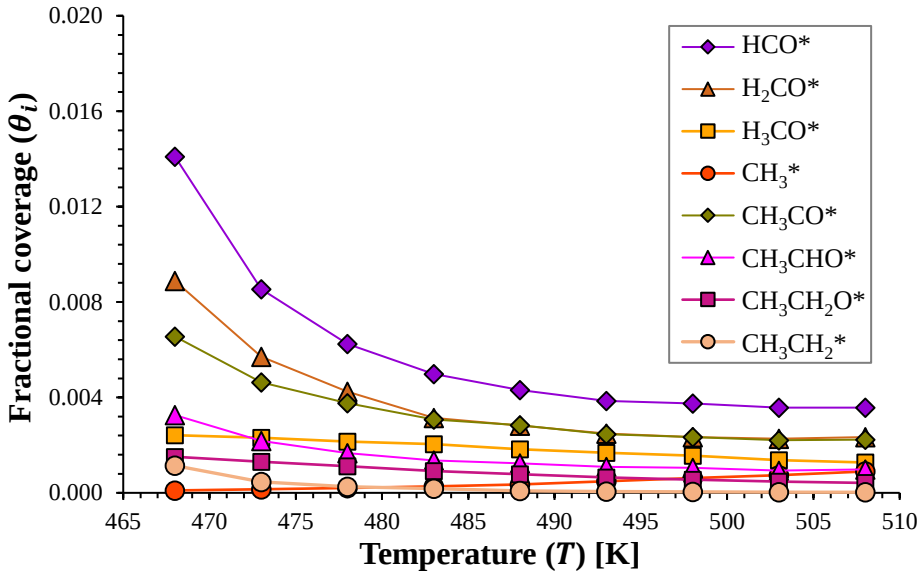

Figure 4.11 Fractional coverages of hydrocarbons as a function of temperature; L = 128, P = 15 bar and H_2/CO = 2.1 (Steady state)

The selectivities of CH_4 and C_2 products as a function of temperature is shown in Figure 4.12. It indicates that the reaction temperature plays an important role in the reaction pathways. According to the result, the selectivity of CH_4 exhibits a positive trend with temperatures, while the selectivity of C_2 exhibits a negative trend. Since the increasing temperature reduces fractional coverages of CO* and hydrocarbon intermediates (Figure 4.9 and 4.11), the chance for hydrocarbon chain growth to produce C_2 is reduced. Therefore, the reaction pathways shift to the formation of CH_4 with increasing temperatures. It can be suggested that the higher temperature is more desirable for terminating the hydrocarbon chain growth to produce light hydrocarbon especially CH_4 gas, while the lower temperature is suitable for enhancing the hydrocarbon chain growth to produce heavier products. These trends are similar to the experimental result of Mansouri *et al*. (2014). It can be said that the results obtained from the simulations can suitably be allowed to explain the kinetic behavior in Fischer-Tropsch synthesis reaction instead of experiments.

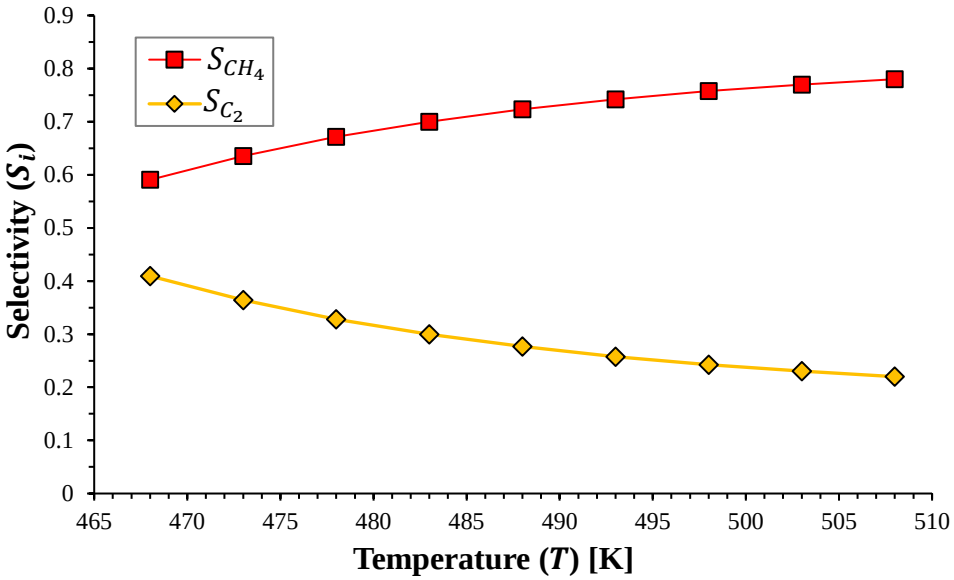

Figure 4.12 Selectivities of CH_4 and C_2 products as a function of temperature; L = 128, P = 15 bar and H_2/CO = 2.1 (Steady state)

4.5 Effect of Reaction Pressure

Due to the assumed infinite reservoir of CO and H_2 gas molecules above the surface of the catalyst, the partial pressures of products can be neglected. Hence, the total reaction pressure consists only of the partial pressures of CO and H_2. In order to investigate the influences of the pressure on the Fischer-Tropsch synthesis reaction, a series of the simulations are performed by varying pressure between 11 and 35 bar at temperature of 493 K and H_2/CO molar ratio in gas feed of 2.1 without inactive impurities on the surface of the catalyst.

Figure 4.13 illustrates the production rates at different pressures between 11 and 35 bar. It can be observed that the production rates of all products increase with increasing reaction pressure. This is because the increase of pressure improves the probability for the collision of reactants to the surface, leading to the increment in fractional coverages of reactants.

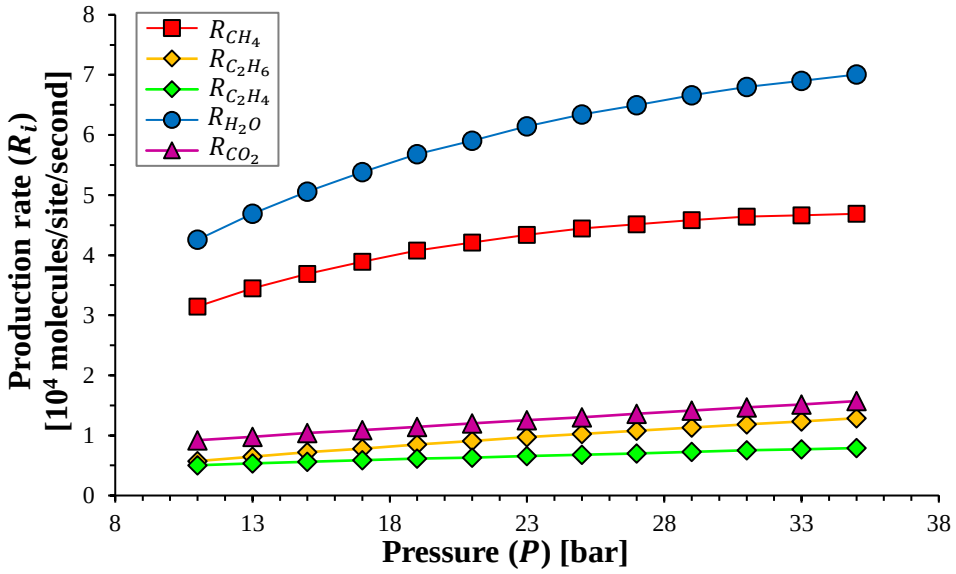

Figure 4.13 Production rates as a function of pressure; $L = 128$, $T = 493$ K and $H_2/CO = 2.1$ (Steady state)

In Figure 4.14, the fractional coverages of CO* and H*, and the fraction of vacant sites as a function of reaction pressure are shown. When the pressure is increased from 11 to 35 bar, the fractional coverage of CO* is obviously increased leading to the reduction of vacant sites on the surface. Although the higher pressure should also enhance the adsorption of H_2, there is only a little bit change for the fractional coverage of H*. This is because the H* species can easily desorb from the surface more than the CO* species. The differences in the equilibrium surface at various pressure can be observed from the snapshots of the surface obtained from the simulations as shown in Figure 4.15. In the Figure 4.15a, at low pressure of 11 bar, the surface exhibits the great number of empty sites. When the pressure is adjusted to 15 and 35 bar as shown in Figure 4.15b and 4.15c respectively, the surfaces are more covered by CO* and the number of vacant sites is obviously decreased.

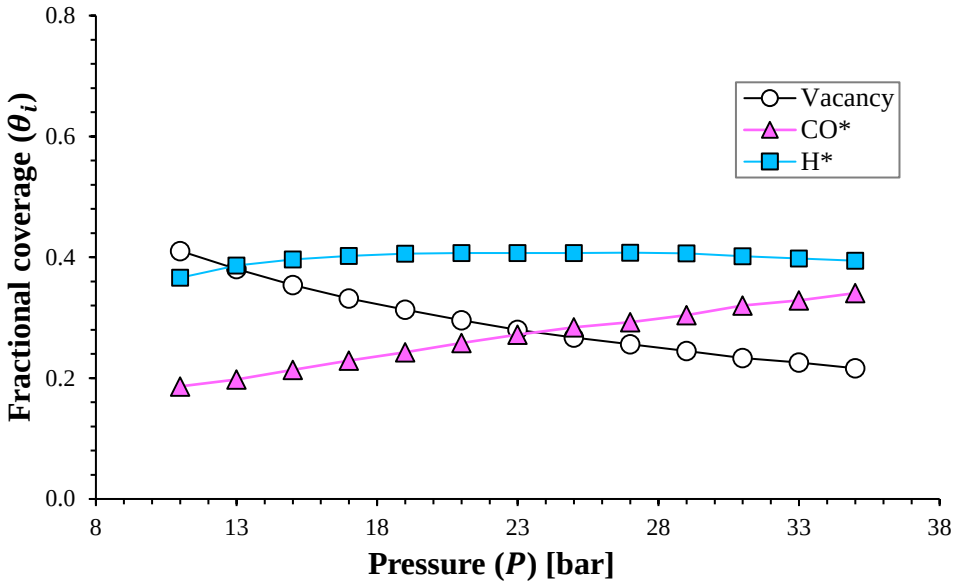

Figure 4.14 Vacant site and fractional coverages of CO* and H* as a function of pressure; $L = 128$, $T = 493$ K and $H_2/CO = 2.1$ (Steady state)

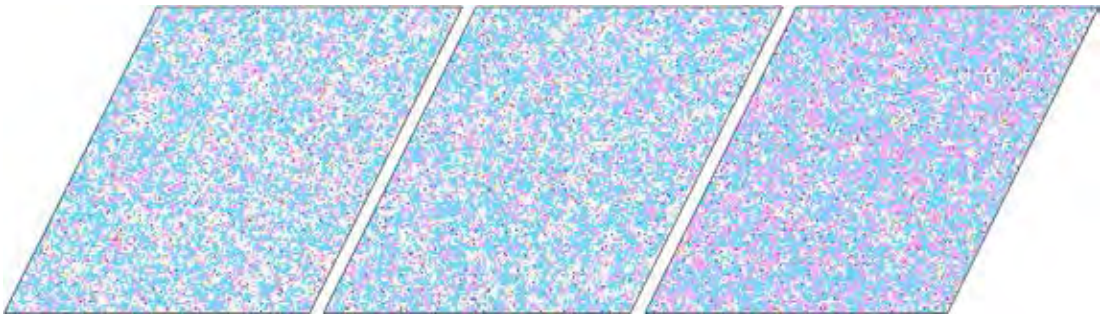

(a) (b) (c)

Figure 4.15 Snapshots of the surface at (a) P = 11 bar, (b) P = 15 bar and (c) P = 35 bar; L = 128, T = 493 K and H_2/CO = 2.1 (□ = Vacant site, ■ = CO*, ■ = H*, ■ = HCO*, ■ = H_2CO*, ■ = H_3CO*, ■ = CH_3*, ■ = CH_3CO*, ■ = CH_3CHO*, ■ = CH_3CH_2O*, ■ = CH_3CH_2*, ■ = O*, ■ = OH*, ■ = H_2O*)

The fractional coverages of adsorbed hydrocarbon species are plotted as a function of reaction pressure in Figure 4.16. It can be observed that the coverages of these species are slightly increased with increasing pressure except CH_3*. They have similar trends to the fractional coverage of CO* (Figure 4.14). It can be indicated that the CO* species can provide the C_1 intermediate species on the surface and can promote the hydrocarbon chain growths to produce C_2 species. Thus, the probability for growing hydrocarbon chains should be increased with increasing pressure because of the longer resident time of these adsorbed hydrocarbon species. The selectivities of hydrocarbon products including CH_4 and C_2 products are presented in Figure 4.17. It can be observed that the reaction pathways shift to produce more C_2 with increasing pressure. The simulation results are strongly agreed with the experimental trends of Todic *et al*. (2016) that the probability for growing hydrocarbon chains can be enhanced due to the increment in adsorbed hydrocarbons species when the reaction pressure is increased.

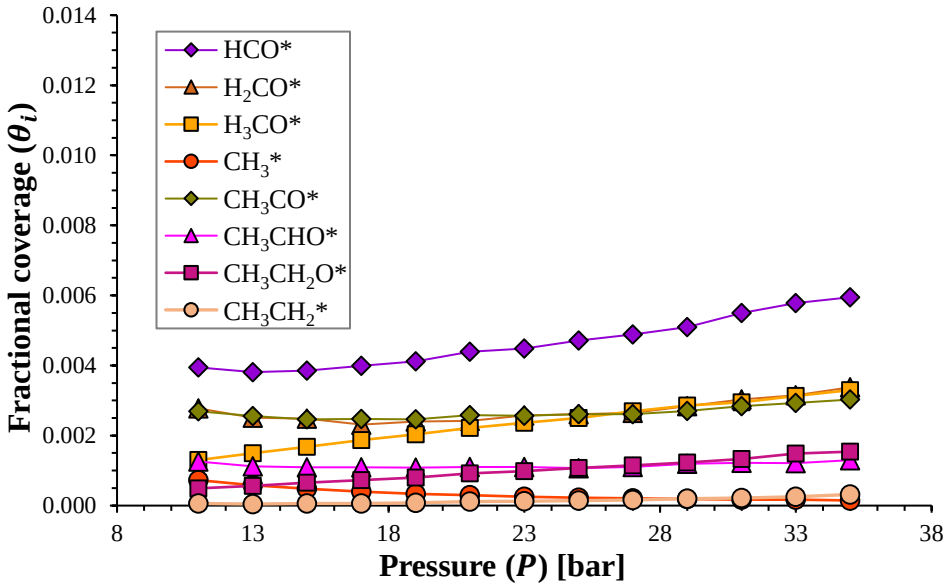

Figure 4.16 Fractional coverages of hydrocarbon intermediates as a function of pressure; $L = 128$, $T = 493$ K and $H_2/CO = 2.1$ (Steady state)

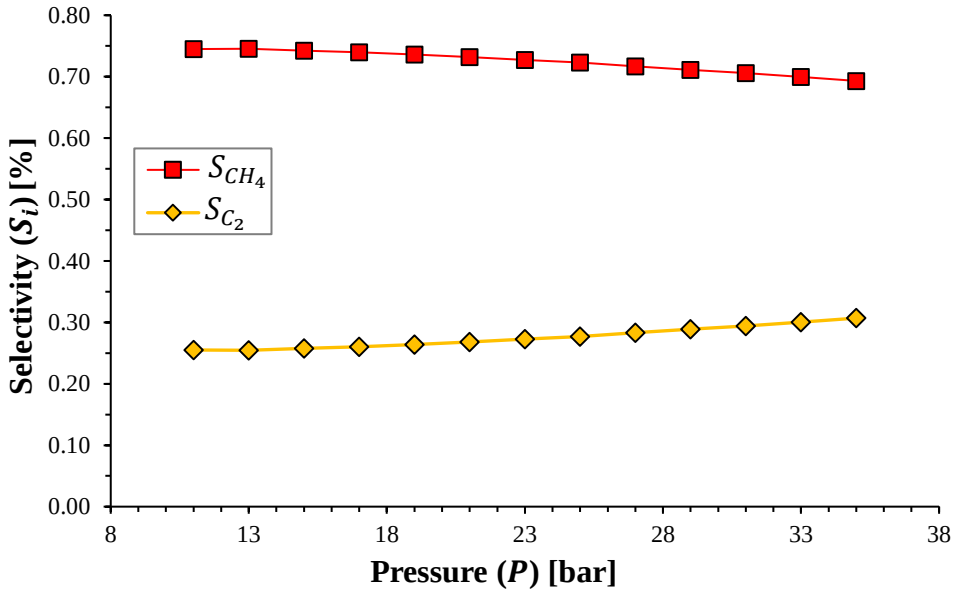

Figure 4.17 Selectivities of CH_4 and C_2 products as a function of pressure; $L = 128$, $T = 493$ K and $H_2/CO = 2.1$ (Steady state)

4.6 Effect of H_2/CO Molar Ratio in Gas Feed

It is well known that the fraction of each reactant in feed significantly play the role for the overall reaction. For the Fischer-Tropsch synthesis reaction, the H_2/CO molar ratio in the gas feed is essentially important. The effects of the H_2/CO ratio on the kinetics are also investigated by adjusting the H_2/CO ratio between 0.6 and 6.1 in the simulations, with fixed temperature of 493 K and pressure of 2.1 bar.

Figure 4.18 shows the production rates as a function of the H_2/CO molar ratio in the gas feed. It can be seen that the reaction cannot take place when the H_2/CO ratio is lower than 1.1. In this range of H_2/CO ratio, the system behaves as unreactive state and the surface of the catalyst is saturated by various adsorbed species. Due to the low H_2/CO ratio or the high proportion of CO in feed, the surface is mostly covered by CO* species. The H* species are not enough to promote the H-assisted dissociation of CO*, which is the initial step in the reaction (step 9 to step 13 in Table 3.2), to provide CH_3*, OH* and O* for the formation of all products. The fractional coverages of CO* and H*, and the fraction of vacant sites at various H_2/CO ratios are depicted in Figure 4.19. It is obviously seen that the CO* species occupy on the surface more than 85% at H_2/CO between 0.6 and 1.1.

The reaction can occur when the ratio of H_2/CO in feed higher than 1.1 (Figure 4.18). In the reactive region, the formation rates of all products are quite high at the ratio of 1.6, and continuously depreciate with increasing H_2/CO feed molar ratio. Nevertheless, the production rates of CH_4 and H_2O slightly rise when the H_2/CO ratio is initially increased from 1.6 to 2.1, while the rates of C_2H_6, C_2H_4 and CO_2 are similar trends to the CO* coverage (Figure 4.19). This is because the CO* species are directly used for the chain growth to form C_2 products and for the Water-Gas Shift to produce CO_2.

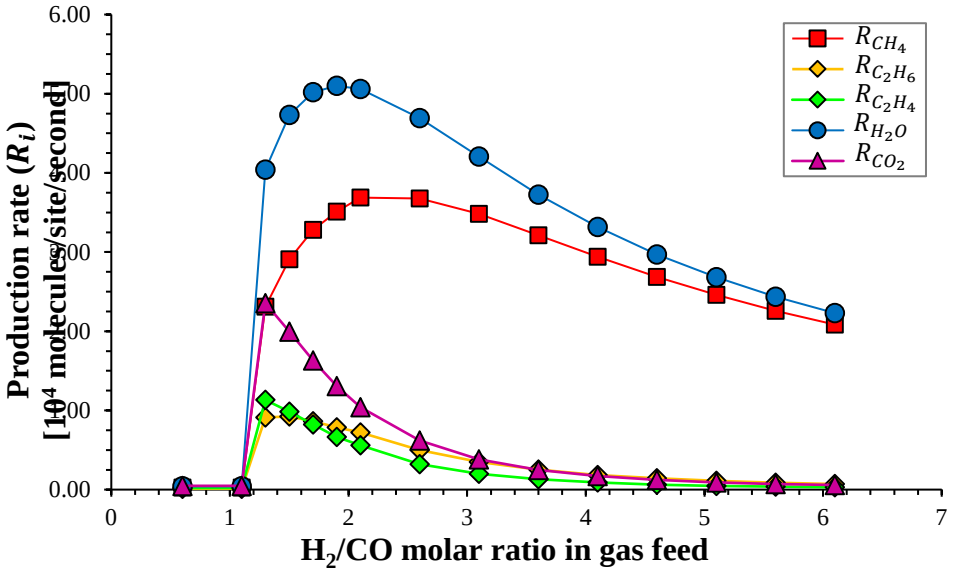

Figure 4.18 Production rates as a function of H_2/CO feed molar ratio; $L = 128$, $T = 493$ K and $P = 15$ bar (Steady state)

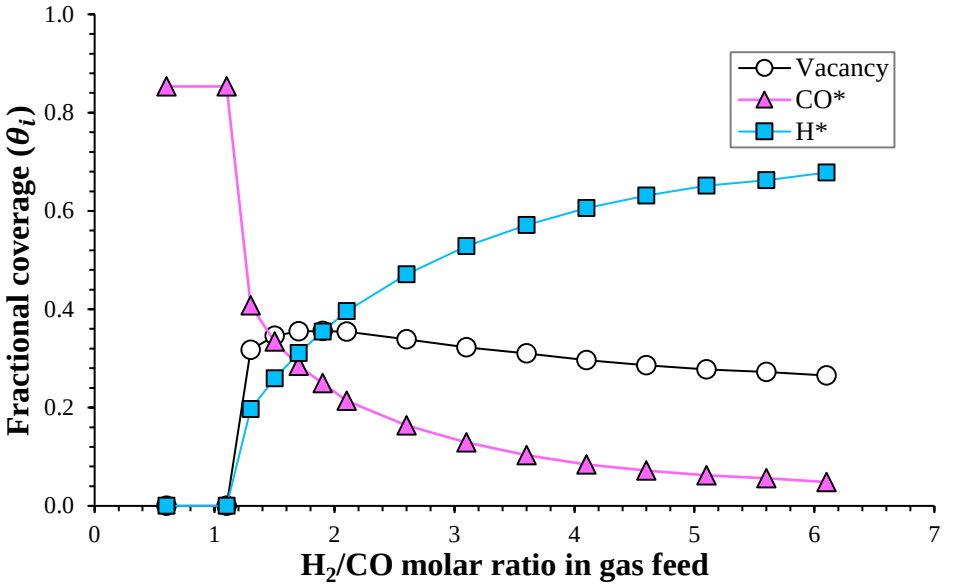

Figure 4.19 Vacant site and fractional coverages of CO* and H* as a function of H_2/CO feed molar ratio; $L = 128$, $T = 493$ K and $P = 15$ bar (Steady state)

The non-reactive state that the surface of the catalyst is only saturated by CO* at the H_2/CO molar feed ratio of 1.1 is clearly seen in Figure 4.20a. Figure 4.20b exhibits a snapshot of the reactive state with the H_2/CO molar ratio of 2.1 in feed. At this condition, the proportion between CO* and H* is appropriate to carry out the surface reactions. The products form continuously and then leave from the surface causing a higher number of vacant sites. At a high H_2/CO ratio of 6.1, the surface is covered mainly with H* as shown in Figure 4.20c. The performance at this condition is very low due to the shortage of CO* which is important to provide the carbon species on the surface.

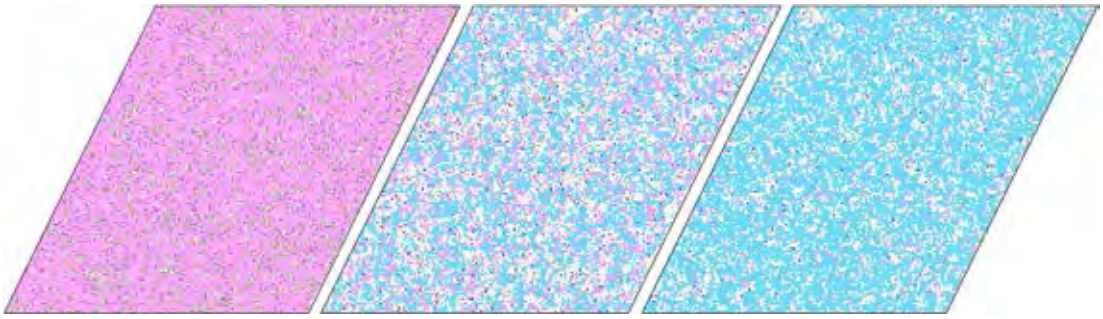

(a) (b) (c)

Figure 4.20 Snapshots of the surface at (a) H_2/CO = 1.1, (b) H_2/CO = 2.1 and (c) H_2/CO = 6.1; L = 128, T = 493 K and P = 15 bar (□ = Vacant site, ■ = CO*, ■ = H*, ■ = HCO*, ■ = H_2CO*, ■ = H_3CO*, ■ = CH_3*, ■ = CH_3CO*, ■ = CH_3CHO*, ■ = CH_3CH_2O*, ■ = CH_3CH_2*, ■ = O*, ■ = OH*, ■ = H_2O*)

The fractional coverages of hydrocarbon species and the selectivities in the reactive state as a function of H_2/CO molar ratio in feed are shown in Figure 4.21 and 4.22, respectively. Since the increment in the ratio of H_2/CO in feed causes to reduce the partial pressure of CO leading to the lack of CO*, the number of the hydrocarbon species on surface is depreciated. As can be seen in Figure 4.21, the fractional coverages of these species rapidly decrease until almost zero when the H_2/CO ratio is increased. Additionally, as an increase of the H_2/CO feed ratio, the decrease in hydrocarbon species on the surface may reduce the probability for the hydrocarbon chain

growth. The C_1 intermediate species are more hydrogenated to make CH_4 before growing to be C_2 species. Thus, the reaction pathways shift to produce CH_4 with increasing H_2/CO ratio. As shown in Figure 4.22, the selectivity of CH_4 exhibits a positive trend while the selectivity of C_2 products exhibits a negative trend with increasing H_2/CO ratio in the feed. Therefore, according to the simulation results, it can be suggested that the higher H_2/CO molar ratio is preferential for terminating the hydrocarbon chain growth to produce light hydrocarbon especially CH_4 gas, while the lower H_2/CO molar ratio is preferential for enhancing the hydrocarbon chain to produce heavier products, as observed in the experimental by Lualdi *et al*. (2012).

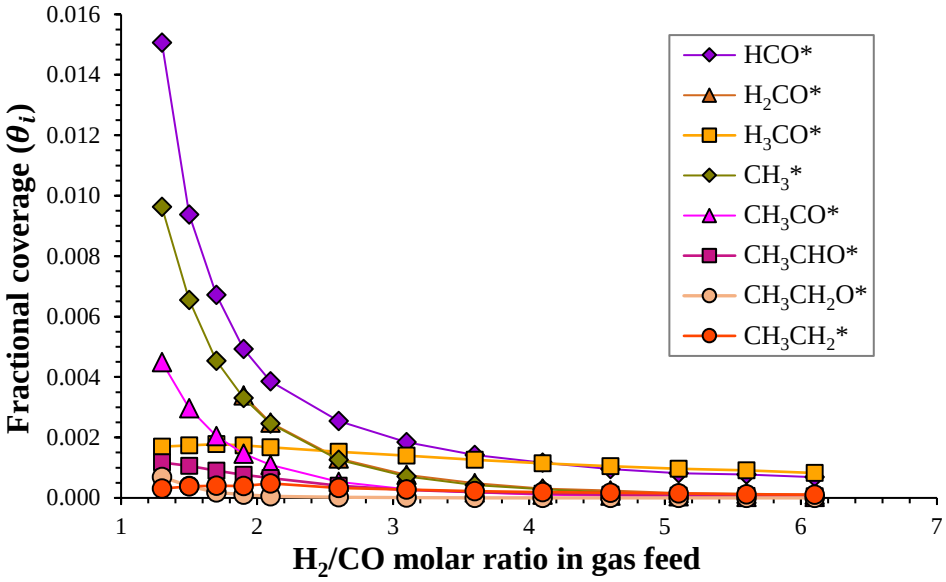

Figure 4.21 Fractional coverages of hydrocarbon intermediates as a function of H_2/CO feed molar ratio; $L = 128$, $T = 493$ K and $P = 15$ bar (Steady state)

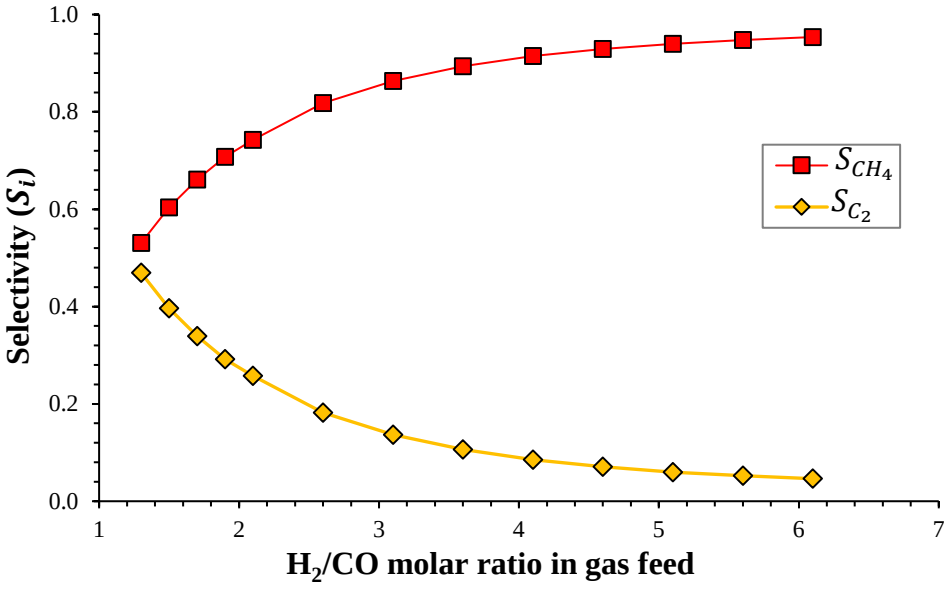

Figure 4.22 Selectivities of CH_4 and C_2 products as a function of H_2/CO feed molar ratio; $L = 128$, $T = 493$ K and $P = 15$ bar (Steady state)

CHAPTER V
CONCLUSIONS AND RECOMMENDATIONS

5.1 Conclusions

The catalytic reaction mechanism and kinetics of C_1 and C_2 formation in the Fischer-Tropsch synthesis over the cobalt catalyst can be investigated by using the KMC simulation. According to the simulation results, the surface of metallic cobalt is covered with the adsorbed H and CO predominantly at the steady state. The proportion of the adsorbed H and CO on the surface of the catalyst plays a significant role in the hydrocarbon chain growth. The investigation of the reaction mechanism shows that the CO insertion mechanism is a suitable kinetic model to describe the Fischer-Tropsch synthesis reaction. It is shown that C–C bond formation for the production of C_2 products is mainly carried out by the insertion of adsorbed CO into a metal–CH_3* bond (step 22 in Table 3.3). Based on the CO insertion mechanism, the effects of reaction condition is examined, and the results obviously present that the reaction temperature, pressure and H_2/CO feed molar ratio certainly control the reactivity and selectivity of the reaction. The production rates of hydrocarbons can be enhanced by increasing the temperature and reactant partial pressure. The increase of H_2/CO ratio in gas feed (low CO) leads to the reduction of reactivity because of the lack of carbon monomer for chain growth. It is observed that the reaction pathways between the production of CH_4 and the formation of C–C bond can also be shifted by adjusting the process conditions. High reaction pressure, high H2/CO feed ratio and low temperature are preferential for enhancing the C–C bond formation, which promotes the probability for growing hydrocarbon chain to produce heavier products. Those trends are strongly agreed with the reported experimental results (Todic *et al*., 2014 and 2016; Lualdi *et al*., 2012; Mansouri *et al*., 2014). Therefore, the simulation results can illustrate the macroscopic kinetics of the Fischer-Tropsch synthesis, which may be useful information for the process design and reaction engineering.

5.2 Recommendations

In this study, the C_1 and C_2 formation in the Fischer-Tropsch synthesis is simulated by using the KMC. The appropriate mechanism is suggested. The effects of reaction temperature, pressure and H_2/CO feed molar ratio are then investigated. Future work for this reaction model would be to expand the formation of hydrocarbon products up to longer chains, to combine with the other approaches for calculation of heavier hydrocarbons, or to study the effects on the supported catalyst.

REFERENCES

Asiaee, A. and Benjamin, K.M. (2017) A density functional theory based elementary reaction mechanism for early steps of Fischer-Tropsch synthesis over cobalt catalyst. 1. Reaction kinetics. Molecular Catalysis, 436, 218–227.

Chen, W., Filot, I.A.W., Pestman, R., and Hensen E.J.M. (2017) Mechanism of Cobalt-Catalyzed CO Hydrogenation: 2. Fischer−Tropsch Synthesis. ACS Catalysis, 7, 8061−8071.

Dry, M.E. (2002) The Fischer–Tropsch process: 1950–2000. Catalysis Today, 71, 227–241.

Gunasooriya, G.T.K.K., Bavel, A.P.V., Kuipers, H.P.C.E., and Saeys, M. (2015) CO adsorption on cobalt: Prediction of stable surface phases. Surface Science, 642, L6–L10.

Hansen, E.W. and Neurock, M. (2000) First-Principles-Based Monte Carlo Simulation of Ethylene Hydrogenation Kinetics on Pd. Journal of Catalysis, 196, 241–252.

Hess, F. and Over, H. (2013, September) Kinetic Monte Carlo Modeling of the HCl Oxidation on RuO_2(110): How Far Can One Get with DFT. Paper presented at 11th European Congress on Catalysis, EuropaCat-XI, Lyon, France.

Jansen, A.P.J. (2012) An introduction to kinetic Monte Carlo simulations of surface reactions. New York: Springer.

Kasht, A., Hussain, R., Ghouri, M., Blank, J., and Elbashir, N.O. (2015) Product Analysis of Supercritical Fischer-Tropsch Synthesis: Utilizing a Unique n-Line and Off-Line Gas Chromatographs Setup in a Bench-Scale Reactor Unit. American Journal of Analytical Chemistry, 6, 659-676.

Li, H., Fu, G., and Xu, X. (2012) A new insight into the initial step in the Fischer–Tropsch synthesis: CO dissociation on Ru surfaces. Physical Chemistry Chemical Physics, 14, 16686–16694.

Liu, J.X., Su, H.Y., Sun, D.P., Zhang, B.Y., and Li, W.X. (2013) Crystallographic Dependence of CO Activation on Cobalt Catalysts: HCP versus FCC. Journal of the American Chemical Society, 135, 16284−16287.

Lualdi, M., Lögdberg, S., Boutonnet, M., and Järås, S. (2013) On the effect of water on the Fischer–Tropsch rate over a Co-based catalyst: The influence of the H2/CO ratio. Catalysis Today, 214, 25-39.

Mansouri, M., Atashi, H., Tabrizi, F.F., Mansouri, G., and Setareshenas, N. (2014) Fischer–Tropsch synthesis on cobalt–manganese nanocatalyst: studies on rate equations and operation conditions. International Journal of Industrial Chemistry, 5, 14-22.

Piccinin, S., and Stamatakis, M. (2014) CO Oxidation on Pd(111): A First-Principles-Based Kinetic Monte Carlo Study. ACS Catalysis, 4, 2143−2152.

Pruksawan, S., Kitiyanan, B., and Ziff, R.M. (2016) Partial oxidation of methane on a nickel catalyst: kinetic Monte-Carlo simulation study. Chemical Engineering Science, 147, 128-136.

Qi, Y., Yang, J., Chen, D., and Holmen, A. (2015) Recent Progresses in Understanding of Co-Based Fischer–Tropsch Catalysis by Means of Transient Kinetic Studies and Theoretical Analysis. Catalysis Letters, 145, 145–161.

Qiu, B., Yang, C., Guo, W., Xu, Y., Liang, Z., Ma, D., and Zou, R. (2017) Highly dispersed Co-based Fischer–Tropsch synthesis catalysts from metal–organic frameworks. Journal of Materials Chemistry A, 5, 8081–8086.

Shetty, S., Jansen, A.P.J., and van Santen, R.A. (2009) Direct versus Hydrogen-Assisted CO Dissociation. Journal of the American Chemical Society, 131, 12874–12875.

Storsæter, S., Chen, D., and Holmen, A. (2006) Microkinetic modelling of the formation of C_1 and C_2 products in the Fischer–Tropsch synthesis over cobalt catalysts. Surface Science, 600, 2051–2063.

Tian, L., Huo, C.F., Cao, D.B., Yang, Y., Xu, J., Wu, B.S., Xiang, H.W., Xu, Y.Y., and Li, Y.W. (2010) Effects of reaction conditions on iron-catalyzed Fischer–Tropsch synthesis: A kinetic Monte Carlo study. Journal of Molecular Structure: THEOCHEM, 941, 30-35.

Todic, B., Ma, W., Jacobs, G., Davis, B.H., and Bukur, D.B. (2014) Effect of process conditions on the product distribution of Fischer–Tropsch synthesis over a Re-promoted cobalt-alumina catalyst using a stirred tank slurry reactor. Journal of Catalysis, 311, 325–338.

Todic, B., Nowicki, L., Nikacevic, N., and Bukur, D.B. (2016) Fischer–Tropsch synthesis product selectivity over an industrialiron-based catalyst: Effect of process conditions. Catalysis Today, 261, 28–39.

Ustinov, E. (2019) Kinetic Monte Carlo approach for molecular modeling of adsorption. Current Opinion in Chemical Engineering, 24, 1–11.

van Santen, R.A., Markvoort, A.J., Filot, I.A.W., Ghouri, M.M., and Hensen, E. J. M. (2013) Mechanism and microkinetics of the Fischer–Tropsch reaction. Physical Chemistry Chemical Physics, 15, 17038-17063.

van Santen, R.A., and Sautet, P. (Eds.). (2009) Computational Methods in Catalysis and Materials Science: An Introduction for Scientists and Engineers. Weinheim: Wiley.

Visconti, C.G., Tronconi, E., Lietti, L., Forzatti, P., Rossini, S., and Zennaro, R. (2011) Detailed Kinetics of the Fischer–Tropsch Synthesis on Cobalt Catalysts Based on H-Assisted CO Activation. Topics in Catalysis, 54, 786–800.

Yang, J., Qi, Y., Zhu, J., Zhu, Y.A., Chen, D., and Holmen, A. (2013) Reaction mechanism of CO activation and methane formation on Co Fischer–Tropsch catalyst: A combined DFT, transient, and steady-state kinetic modeling. Journal of Catalysis, 308, 37–49.

Ziff, R.M., Gulari, E., and Barshad, Y. (1986). Kinetic Phase Transitions in an Irreversible Surface-Reaction Model. Physical Review Letters, 56(24), 2553-2556.

APPENDICES

Appendix A Raw Data of Results

Table A1 Production rates as a function of time from carbide mechanism; T = 493 K, P = 15 bar and H_2/CO = 2.1

Time [millisecond]	**Production rate (R_i)** [10^4 molecules/site/second]				
	R_{CH_4}	$R_{C_2H_6}$	$R_{C_2H_4}$	R_{H_2O}	R_{CO_2}
0.00	0.75	0.00	0.00	0.44	0.03
0.03	4.72	0.06	0.07	4.15	0.85
0.06	4.86	0.08	0.08	4.15	1.03
0.10	4.91	0.08	0.08	4.16	1.08
0.13	4.93	0.08	0.08	4.15	1.11
0.17	4.94	0.08	0.08	4.14	1.14
0.20	4.95	0.08	0.08	4.14	1.14
0.23	4.96	0.08	0.08	4.14	1.15
0.27	4.96	0.08	0.09	4.14	1.16
0.34	4.97	0.08	0.09	4.14	1.17
0.37	4.98	0.08	0.08	4.14	1.17
0.40	4.98	0.08	0.09	4.15	1.17
0.44	4.98	0.08	0.09	4.15	1.18
0.47	4.98	0.08	0.09	4.15	1.18
0.50	4.98	0.08	0.09	4.15	1.18

Table A2 Fraction of vacant site and fractional coverages of adsorbed reactants as a function of time from carbide mechanism; T = 493 K, P = 15 bar and H_2/CO = 2.1

Time [millisecond]	**Fractional coverage (θ_i)**		
	$\boldsymbol{\theta_{Vacant}}$	$\boldsymbol{\theta_{CO}}$	$\boldsymbol{\theta_{H}}$
0.00	0.4326	0.0789	0.4814
0.03	0.3331	0.3087	0.3234
0.06	0.3265	0.3160	0.3193
0.10	0.3216	0.3090	0.3301
0.13	0.3199	0.3270	0.3137
0.17	0.3300	0.3166	0.3167
0.20	0.3125	0.3259	0.3207
0.23	0.3212	0.3176	0.3209
0.27	0.3210	0.3199	0.3206
0.34	0.3290	0.3154	0.3187
0.37	0.3196	0.3138	0.3284
0.40	0.3129	0.3270	0.3251
0.44	0.3216	0.3146	0.3279
0.47	0.3209	0.3203	0.3204
0.50	0.3109	0.3195	0.3309

Table A3 Production rates as a function of time from CO insertion mechanism; T = 493 K, P = 15 bar and H_2/CO = 2.1

Time [millisecond]	**Production rate (R_i)** [10^4 molecules/site/second]				
	R_{CH_4}	$R_{C_2H_6}$	$R_{C_2H_4}$	R_{H_2O}	R_{CO_2}
0.00	0.05	0.00	0.00	0.00	0.00
0.03	3.58	0.61	0.45	4.69	0.83
0.05	3.61	0.68	0.52	4.87	0.96
0.08	3.66	0.69	0.53	4.96	0.98
0.11	3.68	0.70	0.54	4.99	1.00
0.13	3.69	0.70	0.55	5.02	1.01
0.16	3.68	0.70	0.55	5.02	1.02
0.19	3.68	0.71	0.55	5.03	1.02
0.21	3.68	0.71	0.55	5.03	1.03
0.24	3.69	0.71	0.56	5.04	1.03
0.27	3.69	0.71	0.56	5.04	1.03
0.30	3.69	0.71	0.56	5.04	1.04
0.33	3.69	0.71	0.56	5.04	1.03
0.35	3.69	0.71	0.56	5.05	1.04
0.38	3.69	0.72	0.56	5.05	1.04
0.41	3.69	0.72	0.56	5.04	1.04
0.44	3.69	0.72	0.56	5.05	1.04
0.47	3.69	0.72	0.56	5.04	1.04
0.50	3.69	0.72	0.56	5.05	1.04

Table A4 Fraction of vacant site and fractional coverages of adsorbed reactants as a function of time from CO insertion mechanism; T = 493 K, P = 15 bar and H_2/CO = 2.1

Time [millisecond]	**Fractional coverage (θ_i)**		
	$\boldsymbol{\theta_{Vacant}}$	$\boldsymbol{\theta_{CO}}$	$\boldsymbol{\theta_{H}}$
0.00	0.6687	0.0424	0.2876
0.03	0.3627	0.2213	0.3823
0.05	0.3546	0.2156	0.3986
0.08	0.3638	0.2139	0.3909
0.11	0.3500	0.2204	0.3986
0.13	0.3606	0.2157	0.3900
0.16	0.3535	0.2180	0.3942
0.19	0.3613	0.2164	0.3882
0.21	0.3569	0.2205	0.3887
0.24	0.3568	0.2124	0.3972
0.27	0.3512	0.2139	0.4022
0.30	0.3534	0.2183	0.3931
0.33	0.3514	0.2125	0.3996
0.35	0.3508	0.2137	0.4033
0.38	0.3608	0.2082	0.3977
0.41	0.3509	0.2152	0.3982
0.44	0.3447	0.2139	0.4072
0.47	0.3579	0.2192	0.3858
0.50	0.3536	0.2146	0.3958

Table A5 Production rates as a function of time from combination between carbide and CO insertion mechanism; T = 493 K, P = 15 bar and H_2/CO = 2.1

Time [millisecond]	**Production rate (R_i)** [10^4 molecules/site/second]				
	R_{CH_4}	$R_{C_2H_6}$	$R_{C_2H_4}$	R_{H_2O}	R_{CO_2}
0.00	0.00	0.00	0.00	0.00	0.00
0.01	3.01	0.42	0.24	3.89	0.34
0.01	3.25	0.54	0.36	4.47	0.57
0.02	3.33	0.63	0.42	4.69	0.71
0.03	3.37	0.67	0.47	4.86	0.77
0.03	3.39	0.69	0.49	4.93	0.81
0.04	3.38	0.71	0.51	4.96	0.84
0.05	3.39	0.71	0.52	5.00	0.86
0.05	3.40	0.73	0.54	5.05	0.88
0.06	3.40	0.74	0.55	5.07	0.89
0.09	3.41	0.76	0.56	5.13	0.91
0.12	3.41	0.77	0.57	5.16	0.92
0.15	3.41	0.77	0.58	5.18	0.93
0.18	3.42	0.77	0.58	5.19	0.94
0.21	3.42	0.78	0.59	5.19	0.95
0.23	3.42	0.78	0.59	5.20	0.96
0.26	3.42	0.78	0.59	5.21	0.96
0.29	3.42	0.78	0.60	5.21	0.96
0.32	3.42	0.78	0.60	5.21	0.96

Table A6 Fraction of vacant site and fractional coverages of adsorbed reactants as a function of time from combination between carbide and CO insertion mechanism; T = 493 K, P = 15 bar and H_2/CO = 2.1

Time [millisecond]	**Fractional coverage (θ_i)**		
	$\boldsymbol{\theta_{Vacant}}$	$\boldsymbol{\theta_{CO}}$	$\boldsymbol{\theta_{H}}$
0.00	0.8921	0.0140	0.0939
0.01	0.3420	0.1863	0.4499
0.01	0.3515	0.2188	0.4029
0.02	0.3610	0.2186	0.3917
0.03	0.3611	0.2183	0.3954
0.03	0.3516	0.2232	0.3967
0.04	0.3572	0.2310	0.3826
0.05	0.3643	0.2336	0.3729
0.05	0.3688	0.2166	0.3828
0.06	0.3539	0.2227	0.3931
0.09	0.3577	0.2233	0.3909
0.12	0.3687	0.2220	0.3777
0.15	0.3630	0.2243	0.3812
0.18	0.3547	0.2297	0.3832
0.21	0.3574	0.2218	0.3902
0.23	0.3567	0.2236	0.3871
0.26	0.3411	0.2234	0.4051
0.29	0.3590	0.2213	0.3859
0.32	0.3575	0.2205	0.3895

Table A7 Formation rates of C_2 intermediates from the combined carbide and CO insertion mechanism at various conditions

Reaction condition			**Formation rate of C_2 intermediate (R_i)** [10^4 molecules/site/second]			
T [K]	P [bar]	H_2/CO	$R_{CH_3CH^*}$	$R_{CH_3CH_2^*}$	$R_{CH_3CH_3^*}$	$R_{CH_3CO^*}$
493	15	1.4	0.0230	0.0097	0.0017	1.0658
493	15	2.1	0.0544	0.0231	0.0053	1.9860
493	25	2.1	0.0362	0.0158	0.0040	1.7641
503	15	1.4	0.0660	0.0267	0.0086	2.3897
503	15	2.1	0.0331	0.0141	0.0076	1.4472
503	25	1.4	0.0825	0.0349	0.0085	3.1512
503	25	2.1	0.0254	0.0100	0.0047	1.4006

Table A8 Production rates and selectivities of CH_4 and C_2 products from CO insertion mechanism as a function of temperature; L = 128, P = 15 bar and H_2/CO = 2.1

$\boldsymbol{T}$ [K]	**Production rate ($\boldsymbol{R_i}$)**					**Selectivity ($\boldsymbol{S_i}$)**	
	$\boldsymbol{R_{CH_4}}$	$\boldsymbol{R_{C_2H_6}}$	$\boldsymbol{R_{C_2H_4}}$	$\boldsymbol{R_{H_2O}}$	$\boldsymbol{R_{CO_2}}$	$\boldsymbol{S_{CH_4}}$	$\boldsymbol{S_{C_2}}$
453	0.03	0.01	0.01	0.05	0.03	0.58	0.42
458	0.07	0.03	0.03	0.12	0.07	0.54	0.46
463	0.07	0.03	0.03	0.12	0.07	0.54	0.46
468	1.20	0.47	0.37	1.92	0.83	0.59	0.41
473	1.70	0.55	0.42	2.60	0.91	0.64	0.36
478	2.19	0.61	0.46	3.24	0.96	0.67	0.33
483	2.68	0.66	0.49	3.85	0.99	0.70	0.30
488	3.19	0.69	0.53	4.48	1.01	0.72	0.28
493	3.69	0.72	0.56	5.06	1.04	0.74	0.26
498	4.17	0.74	0.60	5.63	1.06	0.76	0.24
503	4.66	0.75	0.64	6.19	1.09	0.77	0.23
508	5.12	0.76	0.68	6.72	1.12	0.78	0.22

Table A9 Vacant site and fractional coverages from CO insertion mechanism as a function of temperature; $L = 128$, $P = 15$ bar and $H_2/CO = 2.1$

T [K]	Fractional coverage (θ_i)										
	θ_{Vacant}	θ_{CO}	θ_{H}	θ_{HCO}	θ_{H_2CO}	θ_{H_3CO}	θ_{CH_3}	θ_{CH_3CO}	θ_{CH_3CHO}	$\theta_{CH_3CH_2O}$	$\theta_{CH_3CH_2}$
453	0.0000	0.8411	0.0000	0.0803	0.0345	0.0005	0.0000	0.0178	0.0079	0.0004	0.0036
458	0.0000	0.8387	0.0000	0.0795	0.0328	0.0005	0.0000	0.0196	0.0094	0.0009	0.0043
463	0.0000	0.8387	0.0000	0.0795	0.0328	0.0005	0.0000	0.0196	0.0094	0.0009	0.0043
468	0.1796	0.4911	0.2668	0.0141	0.0089	0.0024	0.0001	0.0066	0.0033	0.0015	0.0011
473	0.2220	0.4092	0.3188	0.0085	0.0057	0.0023	0.0002	0.0046	0.0022	0.0013	0.0005
478	0.2567	0.3470	0.3522	0.0062	0.0042	0.0022	0.0002	0.0038	0.0017	0.0011	0.0003
483	0.2918	0.2935	0.3751	0.0050	0.0031	0.0020	0.0003	0.0031	0.0014	0.0009	0.0002
488	0.3229	0.2530	0.3862	0.0043	0.0028	0.0018	0.0004	0.0028	0.0012	0.0008	0.0001
493	0.3542	0.2138	0.3962	0.0039	0.0025	0.0017	0.0005	0.0025	0.0011	0.0007	0.0001
498	0.3841	0.1852	0.3949	0.0037	0.0023	0.0016	0.0006	0.0023	0.0010	0.0006	0.0000
503	0.4126	0.1605	0.3925	0.0036	0.0023	0.0014	0.0007	0.0022	0.0009	0.0005	0.0000
508	0.4435	0.1407	0.3824	0.0036	0.0023	0.0013	0.0009	0.0022	0.0010	0.0004	0.0000

Table A10 Production rates and selectivities of CH_4 and C_2 products from CO insertion mechanism as a function of pressure; L = 128, T = 493 K and H_2/CO = 2.1

$\boldsymbol{P}$ [bar]	**Production rate ($\boldsymbol{R_i}$)**					**Selectivity ($\boldsymbol{S_i}$)**	
	$\boldsymbol{R_{CH_4}}$	$\boldsymbol{R_{C_2H_6}}$	$\boldsymbol{R_{C_2H_4}}$	$\boldsymbol{R_{H_2O}}$	$\boldsymbol{R_{CO_2}}$	$\boldsymbol{S_{CH_4}}$	$\boldsymbol{S_{C_2}}$
11	3.15	0.57	0.50	4.26	0.92	0.75	0.25
13	3.45	0.65	0.53	4.69	0.98	0.75	0.25
15	3.69	0.72	0.56	5.06	1.04	0.74	0.26
17	3.89	0.78	0.59	5.38	1.09	0.74	0.26
19	4.07	0.85	0.62	5.68	1.14	0.74	0.26
21	4.21	0.91	0.63	5.90	1.20	0.73	0.27
23	4.34	0.97	0.66	6.14	1.26	0.73	0.27
25	4.45	1.03	0.68	6.34	1.30	0.72	0.28
27	4.51	1.08	0.70	6.49	1.36	0.72	0.28
29	4.59	1.13	0.73	6.66	1.41	0.71	0.29
31	4.64	1.19	0.75	6.80	1.47	0.71	0.29
33	4.66	1.23	0.77	6.90	1.51	0.70	0.30
35	4.69	1.29	0.79	7.01	1.57	0.69	0.31

Table A11 Vacant site and fractional coverages from CO insertion mechanism as a function of pressure; $L = 128$, $T = 493$ K and $H_2/CO = 2.1$

P [bar]	Fractional coverage (θ_i)										
	θ_{Vacant}	θ_{CO}	θ_{H}	θ_{HCO}	θ_{H_2CO}	θ_{H_3CO}	θ_{CH_3}	θ_{CH_3CO}	θ_{CH_3CHO}	$\theta_{CH_3CH_2O}$	$\theta_{CH_3CH_2}$
11	0.4105	0.1864	0.3662	0.0039	0.0028	0.0013	0.0007	0.0027	0.0013	0.0005	0.0001
13	0.3807	0.1978	0.3862	0.0038	0.0025	0.0015	0.0006	0.0026	0.0011	0.0006	0.0000
15	0.3542	0.2138	0.3962	0.0039	0.0025	0.0017	0.0005	0.0025	0.0011	0.0007	0.0001
17	0.3320	0.2289	0.4025	0.0040	0.0023	0.0019	0.0004	0.0025	0.0011	0.0007	0.0001
19	0.3133	0.2430	0.4059	0.0041	0.0024	0.0020	0.0003	0.0025	0.0011	0.0008	0.0001
21	0.2956	0.2579	0.4069	0.0044	0.0024	0.0022	0.0003	0.0026	0.0011	0.0009	0.0001
23	0.2801	0.2720	0.4068	0.0045	0.0026	0.0024	0.0003	0.0026	0.0011	0.0010	0.0001
25	0.2671	0.2841	0.4073	0.0047	0.0026	0.0025	0.0002	0.0026	0.0011	0.0011	0.0001
27	0.2559	0.2926	0.4076	0.0049	0.0027	0.0027	0.0002	0.0026	0.0011	0.0011	0.0002
29	0.2450	0.3041	0.4066	0.0051	0.0028	0.0029	0.0002	0.0027	0.0012	0.0012	0.0002
31	0.2335	0.3202	0.4017	0.0055	0.0030	0.0029	0.0002	0.0028	0.0012	0.0013	0.0002
33	0.2256	0.3286	0.3980	0.0058	0.0031	0.0031	0.0002	0.0029	0.0012	0.0015	0.0003
35	0.2163	0.3407	0.3942	0.0059	0.0034	0.0033	0.0001	0.0030	0.0013	0.0015	0.0003

Table A12 Production rates and selectivities of CH_4 and C_2 products from CO insertion mechanism as a function of H_2/CO feed molar ratio; $L = 128$, $T = 493$ K and $P = 15$ bar

H_2/CO	Production rate (R_i)					Selectivity (S_i)	
	R_{CH_4}	$R_{C_2H_6}$	$R_{C_2H_4}$	R_{H_2O}	R_{CO_2}	S_{CH_4}	S_{C_2}
0.6	0.02	0.01	0.02	0.04	0.05	0.44	0.56
1.1	0.02	0.01	0.02	0.04	0.05	0.44	0.56
1.3	2.31	0.91	1.13	4.04	2.36	0.53	0.47
1.5	2.91	0.92	0.99	4.73	2.00	0.60	0.40
1.7	3.28	0.86	0.82	5.02	1.63	0.66	0.34
1.9	3.51	0.79	0.66	5.10	1.31	0.71	0.29
2.1	3.69	0.72	0.56	5.06	1.04	0.74	0.26
2.6	3.68	0.50	0.32	4.69	0.62	0.82	0.18
3.1	3.48	0.35	0.20	4.21	0.38	0.86	0.14
3.6	3.21	0.25	0.13	3.73	0.25	0.89	0.11
4.1	2.94	0.18	0.09	3.32	0.17	0.91	0.09
4.6	2.68	0.14	0.06	2.97	0.12	0.93	0.07
5.1	2.46	0.11	0.05	2.68	0.09	0.94	0.06
5.6	2.26	0.09	0.04	2.44	0.07	0.95	0.05
6.1	2.09	0.07	0.03	2.23	0.06	0.95	0.05

Table A13 Vacant site and fractional coverages from CO insertion mechanism as a function of H_2/CO feed molar ratio; $L = 128$, $T = 493$ K and $P = 15$ bar

H_2/CO	Fractional coverage (θ_i)										
	θ_{Vacant}	θ_{CO}	θ_{H}	θ_{HCO}	θ_{H_2CO}	θ_{H_3CO}	θ_{CH_3}	θ_{CH_3CO}	θ_{CH_3CHO}	$\theta_{CH_3CH_2O}$	$\theta_{CH_3CH_2}$
0.6	0.0000	0.8532	0.0000	0.0623	0.0290	0.0005	0.0000	0.0255	0.0120	0.0001	0.0038
1.1	0.0000	0.8532	0.0000	0.0623	0.0290	0.0005	0.0000	0.0255	0.0120	0.0001	0.0038
1.3	0.3172	0.4077	0.1970	0.0151	0.0102	0.0017	0.0003	0.0096	0.0045	0.0012	0.0007
1.5	0.3463	0.3343	0.2596	0.0094	0.0066	0.0017	0.0004	0.0065	0.0030	0.0011	0.0004
1.7	0.3554	0.2846	0.3110	0.0067	0.0047	0.0018	0.0004	0.0045	0.0020	0.0009	0.0002
1.9	0.3555	0.2499	0.3542	0.0049	0.0034	0.0017	0.0004	0.0033	0.0015	0.0008	0.0001
2.1	0.3542	0.2138	0.3962	0.0039	0.0025	0.0017	0.0005	0.0025	0.0011	0.0007	0.0001
2.6	0.3391	0.1636	0.4711	0.0025	0.0013	0.0015	0.0003	0.0013	0.0005	0.0004	0.0000
3.1	0.3226	0.1288	0.5285	0.0018	0.0008	0.0014	0.0003	0.0007	0.0003	0.0003	0.0000
3.6	0.3104	0.1029	0.5713	0.0014	0.0005	0.0013	0.0002	0.0004	0.0002	0.0002	0.0000
4.1	0.2967	0.0841	0.6059	0.0012	0.0003	0.0011	0.0002	0.0003	0.0001	0.0001	0.0000
4.6	0.2861	0.0719	0.6311	0.0010	0.0002	0.0010	0.0002	0.0002	0.0001	0.0001	0.0000
5.1	0.2775	0.0618	0.6511	0.0008	0.0002	0.0010	0.0001	0.0001	0.0001	0.0001	0.0000
5.6	0.2723	0.0564	0.6625	0.0008	0.0001	0.0009	0.0001	0.0001	0.0000	0.0001	0.0000
6.1	0.2655	0.0486	0.6781	0.0007	0.0001	0.0008	0.0001	0.0001	0.0000	0.0001	0.0000

Appendix B Java code

The java codes that were utilized to perform the reaction mechanism, including the carbide mechanism, the CO insertion mechanism and the combined carbide and CO insertion mechanism, are available as https://github.com/pnuttawut/KMC-code.

CURRICULUM VITAE

Name: Ms. Nuttawut Pugingna

Date of Birth: May 12, 1994

Nationality: Thai

University Education:

2013–2017 Bachelor Degree of Chemical Engineering, Faculty of Engineering, Burapha University, Chonburi, Thailand

Work Experience:

2016	Position:	Technologist Trainee
	Company name:	Thai Oil Public Company Limited

Proceedings:

1. Pugingna, N., Kitiyanan, B., and Ziff, R.M. (2019, May 30) Kinetics Study for Fischer-Tropsch Synthesis over Cobalt Catalyst by Kinetic Monte Carlo Simulation. Proceedings of the 25th PPC Symposium 2019, Bangkok, Thailand.

Presentations:

1. Pugingna, N., Dechakumpoo, K., Kitiyanan, B., and Ziff, R.M. (2018, October 12) Kinetic Monte-Carlo Simulation of Methane Reforming by Carbon Dioxide Using Nickel Catalyst. Poster presented at the International Symposium on Catalysis and Fine Chemicals 2018, Bangkok, Thailand.
2. Pugingna, N., Kitiyanan, B., and Ziff, R.M. (2019, May 30) Investigation of Fischer-Tropsch Synthesis Mechanism over Cobalt Catalyst by Kinetic Monte Carlo Simulation. Poster presented at the 25th PPC Symposium 2019, Bangkok, Thailand.